



Tectonics*

RESEARCH ARTICLE

10.1029/2023TC007885

Key Points:

- · Basal sediments in the Linfen Basin (LB) yield ~4.2 and ~6.1 Ma burial ages, indicating diachronous, northward-propagating extension
- Fault-bend folding theory-based seismic interpretation yields ~3.6 km extension at a mean rate of ~0.9 km/ Myr across the basin
- The LB of the Shanxi Rift System may be a natural example of the lower lithospheric counterflow model

Supporting Information:

Supporting Information may be found in the online version of this article.

Correspondence to:

supeng@ies.ac.cn

Citation:

Su, P., He, H., Liu, Y., Shi, F., Granger, D. E., Kirby, E., et al. (2023). Quantifying the structure and extension rate of the Linfen Basin, Shanxi Rift System since the latest Miocene: Implications for continental magma-poor rifting. Tectonics, 42, e2023TC007885. https:// doi.org/10.1029/2023TC007885

Received 11 APR 2023 Accepted 7 SEP 2023

Author Contributions:

Conceptualization: Peng Su Formal analysis: Peng Su, Yiduo Liu, Darryl E. Granger Funding acquisition: Peng Su, Honglin

He, Feng Shi

Investigation: Peng Su, Feng Shi, Darryl E. Granger, Lan Luo, Fei Han Methodology: Peng Su, Darryl E.

Granger

Project Administration: Peng Su, Honglin He, Feng Shi

Software: Peng Su Supervision: Peng Su, Honglin He, Eric

Kirby Validation: Peng Su Visualization: Peng Su Writing - original draft: Peng Su Writing - review & editing: Peng Su, Honglin He, Yiduo Liu, Eric Kirby,

Renai Lu

© 2023. American Geophysical Union. All Rights Reserved.

Quantifying the Structure and Extension Rate of the Linfen Basin, Shanxi Rift System Since the Latest Miocene: **Implications for Continental Magma-Poor Rifting**

Peng Su^{1,2}, Honglin He^{1,2}, Yiduo Liu³, Feng Shi^{1,2}, Darryl E. Granger^{4,5}, Eric Kirby⁶, Lan Luo⁵, Fei Han⁷, and Rengi Lu¹

¹State Key Laboratory of Earthquake Dynamics, Institute of Geology, China Earthquake Administration, Beijing, China, ²Shanxi Taiyuan Continental Rift Dynamics National Observation and Research Station, Taiyuan, China, ³Key Laboratory of Mountain Hazards and Surface Processes, Institute of Mountain Hazards and Environment, Chinese Academy of Sciences, Chengdu, China, ⁴Department of Earth, Atmospheric, and Planetary Sciences, Purdue University, West Lafayette, IN, USA, 5Department of Physics, Purdue Rare Isotope Measurement Laboratory, Purdue University, West Lafayette, IN, USA, ⁶Department of Earth, Marine and Environmental Sciences, University of North Carolina, Chapel Hill, NC, USA, ⁷Yunnan Key Laboratory of Earth System Science, Yunnan University, Kunming, China

Abstract The formation of magma-poor continental rifts is an enigmatic process, as the weakening mechanism(s) for cratonic lithosphere remains uncertain in the absence of elevated lithospheric temperature. One view links weakening to melts hidden at depth, while another ascribes it to pre-existing weaknesses. Long-term extensional rates also influence lithospheric strength and rift evolution. We target the Linfen Basin (LB) in the magma-poor Shanxi Rift System (SRS) in the North China Craton to understand these components. We apply cosmogenic ²⁶Al/¹⁰Be burial dating on 14 core samples at different depths from three deep boreholes in the basin and obtain six valid burial ages ranging from 2.37^{+1.18/-1.21} to 5.86^{+inf/-1.37} Ma. We further re-interpret a seismic reflection profile and quantify the geometry and amount of extension by forward structural modeling with multiple constraints based on extensional fault-bend folding theory. The timing of the basal sedimentation is estimated to be ~ 6.1 and ~ 4.2 Ma in the southern and northern portions, respectively, indicating diachronous, northward-propagating rifting. The amount and mean rate of extension are ~3.6 km and ~0.9 km/Myr, respectively. The basin depths increasing northward indicates the clockwise rotation of the basin. We propose a basin-scale non-rigid transtensional bookshelf faulting model to explain the rotation patterns of the circum-Ordos basins. We argue that the inherited structures weaken the cratonic lithosphere of the SRS, and the low extension rate contributes to its magma-poor nature. We propose a lithospheric-scale evolution model for the LB, invoking the inherited crustal weakness, low extension rate, and lower lithosphere counterflow.

Plain Language Summary Continental rifting is an important part of plate tectonics. Scientists are still trying to understand how magma-poor continental rifts happen because the tectonic forces available are not enough to stretch the strong lithosphere (outer layer of the Earth). We take the Linfen Basin (LB) in the magmapoor Shanxi Rift System (SRS) in North China as an example to study this issue. We find the basin bottom ages are about 6.1 million years in the south and 4.2 million years in the north, indicating northward propagation of the rift basin. The basin extended by about ~3.6 km at an average rate of 0.9 km per million years. Not only the LB but also the circum-Ordos basins are rotating accordantly. We propose a basin-scale non-rigid transtensional bookshelf faulting model to explain their rotation pattern. We argue that the pre-existing, old structures made the SRS's lithosphere weaker, and the slow extension rate contributes to its magma-poor nature. We finally propose a model for how the LB developed over time, which takes into account the crustal weakness caused by the pre-existing structures, slow extension rate, and counterflow in the lower lithosphere.

1. Introduction

Continental rifting is a fundamental phase of the Wilson Cycle and provides insight into the early stage of continental breakup. One central paradox of continental rifting is that available tectonic forces alone cannot extend the strong cratonic lithosphere (Buck, 2004). Magmatism can weaken the lithosphere and reduce the required force, a widely invoked mechanism to explain continental rifting (e.g., Buck, 2004). However, this model cannot easily explain the formation of magma-poor rifts. One view proposes that melts are emplaced primarily at depth, although little or no melts reach the surface in magma-poor rifts (e.g., Buck, 2004; Muirhead et al., 2016).

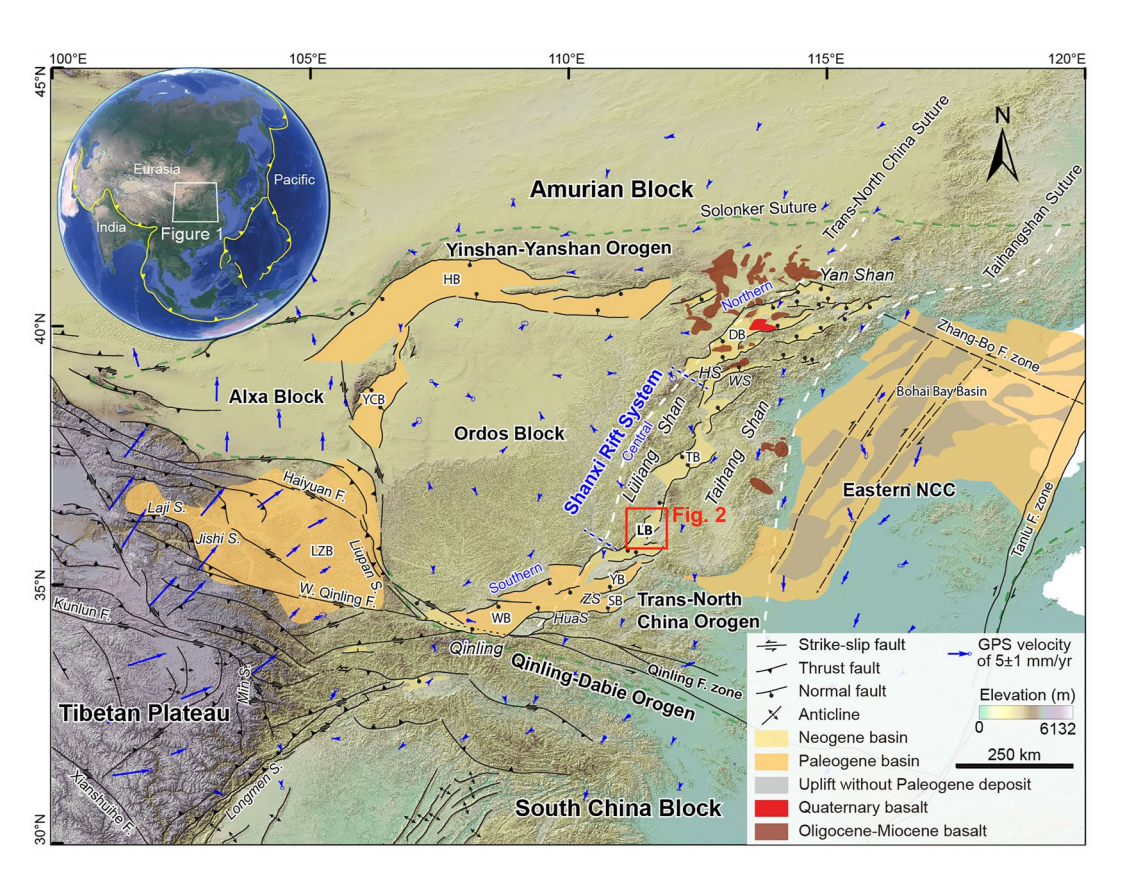


Figure 1. Regional topographic and neotectonic map of North China (modified after Su et al., 2021). The red box shows the location of the study area. Basalt data are modified from Y.-J. Tang et al. (2006). Blue arrows show the GPS velocity field relative to the Ordos Block (simplified from Hao et al., 2021). Dashed blue lines define the boundaries of the northern, central, and southern Shanxi Rift System. Dashed green lines enclose the North China Craton (G. Zhao et al., 2005). Abbreviations: NCC, North China Craton; DB, Datong Basin; HB, Hetao Basin; LB, Linfen Basin; LZB, Longzhong Basin; SB, Sanmenxia Basin; TB, Taiyuan Basin; WB, Weihe Basin; YB, Yuncheng Basin; YCB, Yinchuan Basin; HuaS, Hua Shan; HS, Heng Shan; WS, Wutai Shan; ZS, Zhongtiao Shan. "F." means fault. "S." means Shan or Mountains.

The other school of thought suggests that pre-existing structures weaken the strong lithosphere (e.g., Dunbar & Sawyer, 1988; Peace et al., 2018). Besides these intrinsic factors, the rift extension rate at a geological timescale also influences the lithospheric strength (e.g., Bassi, 1991, 1995; Brun, 1999; Buck, 1991; Dias et al., 2015; England, 1983; Huismans & Beaumont, 2003). Numerical modeling finds that the rift's lithosphere necking zone weakens at a high extension rate, but can regain its strength and become stronger than surrounding domains at a sufficiently low rate (van Wijk & Cloetingh, 2002). Therefore, to understand the formation of a magma-poor rift, one needs to consider factors including the magmatism at depth, pre-existing structures, and extension rate.

The Shanxi Rift System (SRS) is a tectonically active continental rift in the central North China Craton (NCC) (Figure 1) (e.g., X. Xu & Ma, 1992; G. Zhao et al., 2005). While Oligo-Miocene basalts are found in and around the rift, and Quaternary volcanoes exist at the northern end of the rift system (e.g., Y.-J. Tang et al., 2006), the majority of the SRS is magma-poor throughout the Cenozoic. In fact, volcanism in the SRS is arguably more restricted than that of the Rio Grande Rift or the Baikal Rift (e.g., Buck, 1991; Ivanov et al., 2015; Y. Liu et al., 2019). How such a magma-poor rift evolves into a prominent structure remains an open question. The LB in the south-central SRS offers an opportunity to investigate the roles of magmatism, pre-existing structures, and extension rates. A large variety of geophysical observations, for example, controlled source seismic experiments (e.g., S. Li et al., 2011; Z. Li et al., 2014), receiver functions (e.g., Cai et al., 2021; L. Chen et al., 2014; Z. Wei et al., 2011; Y. Zhang et al., 2019), tomography (Dou et al., 2021; Ling et al., 2017; Y. Tang et al., 2010), and magnetotelluric sounding (Y. Yin et al., 2017) provide insights into the lithospheric configuration of the basin. Moreover, pre-rift structures such as Paleoproterozoic shear zones and Mesozoic thrusts have been mapped in the Shanxi region (e.g., B. Zhang et al., 2021; G. Zhao et al., 2005). The parallelism between the rift-bounding normal faults and the pre-existing structures implies tectonic inheritance during the development of the SRS (Su

SU ET AL. 2 of 22

et al., 2021). However, one missing piece regarding the SRS's tectonics is the extension rate. Obtaining the long-term extension rate of the basin requires a quantitative constraint of the total amount of extension and the age of the initial syn-rift deposits. Nevertheless, they remain poorly constrained in the study area (e.g., Shi et al., 2020; SSB, 1988; X. Xu & Ma, 1992).

This study aims to quantify the crustal-scale cross-sectional geometry, and the amount, timing, and rates of extension of the LB. We first apply cosmogenic ²⁶Al/¹⁰Be burial dating (Granger et al., 1997) on 14 core samples from three new boreholes to constrain the timing of the basin extension. We then conduct quantitative structural modeling with multiple constraints, including surface geology, 17 boreholes, and a deep seismic-reflection profile, to delineate the crustal structures and calculate the total extension across the basin. Combining with published geological and geophysical constraints on the lithospheric structure beneath the LB (e.g., L. Chen et al., 2014; Ling et al., 2017; B. Zhang et al., 2021), we attempt to develop a lithospheric-scale evolution model for the LB.

2. Geological Setting

The SRS is situated in the Trans-North China Orogen in the central NCC (Figure 1). The NCC was amalgamated by two Archean blocks along the Trans-North China Orogen in the Paleoproterozoic (Figure 1) (G. Zhao et al., 2005). The region experienced relatively constant deposition of shallow marine rocks from the Mesoproterozoic to the Early Paleozoic (Meng et al., 2011), which was followed by collisional and transpressional orogenesis in the eastern NCC during the late Mesozoic (Wu et al., 2019; Zhu et al., 2011). During the Middle-Late Jurassic to the earliest Cretaceous (~165–136 Ma), the Yanshanian orogeny generated a suite of NE-trending basement-involved long-wavelength folds in the SRS region (Clinkscales & Kapp, 2019; Davis et al., 2001; Dong et al., 2008). The folds in the Lüliang Shan are typically asymmetric monoclines whose limbs are nearly planar, and the reverse-sense deformation is concentrated in narrow shear zones (B. Zhang et al., 2021; H. Zhao et al., 2020). The SRS region underwent tectonic quiescence with slow exhumation during the Cretaceous to Paleocene (e.g., Clinkscales et al., 2021; Su et al., 2021).

The SRS initiated in the Eocene, forming the Weihe and Yuncheng Basins (YB) in the south (Bellier et al., 1988; S. Fan et al., 2020; Su et al., 2021) (Figure 1). The onset time of the SRS is coeval with a phase of widespread extension in East Asia (Allen et al., 1997; L.-G. Fan et al., 2019; J. Ren et al., 2002; W. Wang et al., 2013; Yin, 2010) that is triggered by the trench-parallel Izanagi-Pacific ridge subduction (Su et al., 2021), or alternatively, the India-Eurasia convergence (e.g., Molnar & Tapponnier, 1975) (Inset in Figure 1). Following a period of tectonic quiescence from the Oligocene to the middle Miocene, the SRS was reactivated in the late Miocene in response to the eastward expansion of the Tibetan Plateau (Peltzer et al., 1985; Su et al., 2021; X. Xu & Ma, 1992). The current SRS consists of a series of left-stepping *en échelon* grabens, separating the Lüliang Shan Mountains to the west from the Taihang Shan Mountains to the east. The rift system contains only sparse volcanic deposits, restricted to Quaternary basalts in the Datong Basin (DB) and Oligo-Miocene basalts in and around the northern rift area (Y.-J. Tang et al., 2006). The Weihe Basin (WB), YB, and some local parts in the southern LB contain Eocene deposits (Bellier et al., 1988; S. Fan et al., 2020; J. Zhao et al., 2019). However, from the LB to the north, the observed bottom syn-rift sedimentary rocks are late Miocene-Pliocene in age (Shi et al., 2020; SSB, 1988; X. Xu & Ma, 1992) (Figure 1).

The LB is a northwestward tilted half-graben, bounded to the west by the NE-striking Luoyun Shan Fault (LSF) (Figure 2) (Z. Li et al., 2014). Basement rocks in the Linfen region consist of the Neoarchean-Paleoproterozoic metamorphic Huoxian and Taiyueshan Groups (SPGEB, 1975–1978; G. Zhao et al., 2008). The basement rocks are overlain by the Neoproterozoic Changcheng Group in angular unconformity. Upward, Cambrian-Ordovician strata mainly consist of limestone and carbonate facies. They are overlain disconformably by Carboniferous-Triassic strata, which consist of continental sandstone, siltstone, mudstone, and shale (SPGEB, 1975–1978; H. Zhao et al., 2020). The LB is predominantly filled with fluvial, alluvial, and eolian sediments during the syn-rifting process (SSB, 1988).

The west-verging Lishi thrust fault juxtaposes the Paleozoic over the Triassic rocks in the Luoyun Shan, marking the Mesozoic Yanshanian orogeny in this region (e.g., B. Zhang et al., 2021; H. Zhao et al., 2020). Away from the Lishi fault, the exposed Permian-Ordovician strata generally have low dip angles (<10°). On the eastern shoulder of the LB, the exposed Triassic-Ordovician strata are also nearly horizontal, dipping gently to the northwest adjacent to the basin (Figure 2).

SU ET AL. 3 of 22

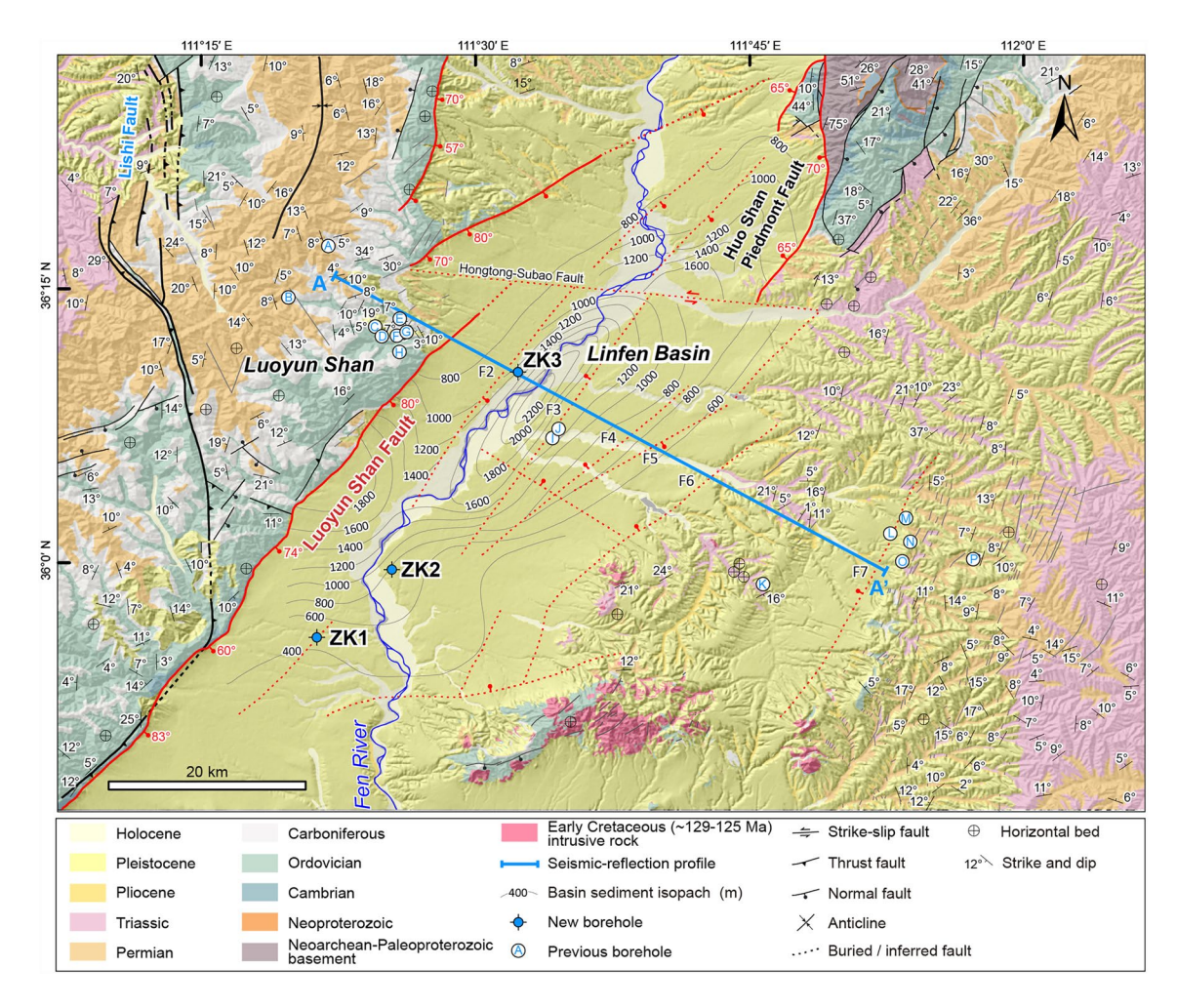


Figure 2. Geologic map of the Linfen Basin region with locations of newly (ZK1–ZK3) and collected boreholes (A–P). See Figure 1 for location. The map is compiled from 1:200,000 geologic maps of the China Geological Survey (SPGEB, 1975–1978). Syn-rift faults are denoted in red and pre-rift faults in black. Intrabasin faults are modified from Z. Li et al. (2014). The basin sediment isopachs are modified from Deng et al. (1993). The age of the Early Cretaceous intrusive rocks is from Yang et al. (2017).

The border LSF controls the shape of the LB, and slip along this bounding fault appears to be primarily dip-slip, normal sense displacement (SSB, 1988). Within the basin, a transfer fault of the Hongtong-Subao Fault intersects the LSF in the north, and several synthetic and antithetic faults parallel to the LSF cut the late Quaternary syn-rift sediments. Almost all the extension strain has been accommodated by the border LSF compared with these intrabasin faults (Figure 2) (Z. Li et al., 2014).

3. Methods and Data

3.1. ²⁶Al/¹⁰Be Burial Dating of Deep Drill Core Samples

3.1.1. Sampling Strategy

We use burial dating with cosmogenic 26 Al and 10 Be to constrain the timing of basin sedimentation. Burial dating is based on the radioactive decay of 26 Al and 10 Be in quartz (Granger et al., 1997). Quartz accumulates 26 Al and 10 Be at a constant ratio during exposure near the ground surface (Lal & Arnold, 1985). Upon deep burial, cosmogenic nuclide production effectively ceases, and the concentrations of the inherited 26 Al and 10 Be decrease by radioactive decay at different rates. Because 26 Al ($t_{1/2} = 0.708 \pm 0.056$ Myr; Nishiizumi, 2004) decays faster than 10 Be ($t_{1/2} = 1.387 \pm 0.012$ Myr; Chmeleff et al., 2010; Korschinek et al., 2010), the 26 Al/ 10 Be ratio decreases exponentially over time and records the duration since the burial. Burial dating with 26 Al and 10 Be is limited to ages within the past \sim 5–6 Myr; beyond this time any inherited 26 Al will have decayed below detection limits. After typically \sim 8 Myr 10 Be will have decayed beyond detection limits.

SU ET AL. 4 of 22

Table 1Burial Ages From ²⁶Al and ¹⁰Be in Borehole Sediments

Sample	Depth (m)		²⁶ Al (10 ⁴ atoms/g)	¹⁰ Be (10 ⁴ atoms/g)	²⁶ Al/ ¹⁰ Be	Burial age (Ma)
ZK1 (35°55′5	56″N, 111°21′2	20″E)				
S06	330.0		1.651 ± 0.478	2.623 ± 0.199	0.63 ± 0.19	4.91+0.86/-0.63
S05	345.4		1.037 ± 0.313	1.271 ± 0.122	0.82 ± 0.26	4.39+0.93/-0.68
S03	390.4		0.548 ± 0.265	1.345 ± 0.131	0.41 ± 0.20	$5.82^{+inf/-0.96}$
S02	429.0		0.384 ± 0.192	0.935 ± 0.254	0.41 ± 0.23	
S01	433.2	434.2 ± 5.7	0.426 ± 0.335	0.630 ± 0.133	0.68 ± 0.55	$5.86^{+inf/-1.37}$
S07	440.3		0.333 ± 0.262	0.343 ± 0.157	0.97 ± 0.88	
ZK2 (35°59′3	39″N, 111°25′2	25″E)				
YC01 ^a	769.0		0.093 ± 0.152	0.094 ± 0.097	0.99 ± 1.93	-
YC02 ^a	769.3		0.330 ± 0.165	0.094 ± 0.068	3.50 ± 3.07	-
ZK3 (36°10′2	26″N, 111°32′	19″E)				
WQ01	1,060.8		1.197 ± 0.379	0.552 ± 0.181	2.17 ± 0.99	2.37+1.18/-1.21
WQ02a	1,065.4		0.238 ± 0.228	0.495 ± 0.120	0.48 ± 0.48	_
WQ04 ^a	1,115.8		1.055 ± 0.374	0.044 ± 0.087	24.06 ± 48.39	-
WQ08	1,143.8	$1,144.0 \pm 0.1$	0.302 ± 0.237	0.199 ± 0.179	1.52 ± 1.81	$2.86^{+1.41/-1.21}$
WQ05	1,144.1		0.509 ± 0.208	0.287 ± 0.091	1.78 ± 0.92	
WQ09 ^a	1,144.3		0.234 ± 0.224	0.261 ± 0.095	0.90 ± 0.92	_

Note. Uncertainties are stated as 1 standard error of the measurement.

^aSamples not used for age determination, as their nuclide concentrations are too low to give the true age of the deposit. ¹⁰Be measurements adjusted to the standard by Nishiizumi et al. (2007), and ²⁶Al measurements to the standard by Nishiizumi (2004).

We acquired samples from discontinuous coring from three deep boreholes (i.e., ZK1, ZK2, and ZK3) in the LB (Figure 2). All three boreholes penetrated the syn-rift sediments and reached the pre-rift strata (Figures S1–S3 in Supporting Information S1; Table 1). We chose medium-coarse quartz sand of fluvial origin to ensure exposure before burial. In each borehole, we collected the available drill cores closest to the basin bottom and a suite of samples at various shallower depths (Figure 3; Table 1).

We obtained 14 core samples in total from the three boreholes (Figure 3; Table 1). The syn-rift sediments in borehole ZK1 are 440.90 m thick, consisting of unconsolidated clay, silt, sand, and gravel. The drilled pre-rift strata are Triassic to Ordovician sedimentary rocks. Three-meter-thick layers of pebbles with coarse sand overlay the Triassic sandstone at the bottom of the basin (Figure S1 in Supporting Information S1). We collected six samples in ZK1 at depths of 330.0 m (S06), 345.4 m (S05), 390.4 m (S03), and 429.0–440.3 m (S02, S01, and S07). The deepest sample S07 consists of fine pebbles with silt and coarse sand; the other samples are silt and sand (Figure 3 and Figure S1 in Supporting Information S1; Table 1).

In borehole ZK2, the syn-rift sediments are 786.8 m thick, and the underlying strata are Triassic to Permian. The available drill cores of the syn-rift sediments are fine sand at a depth of 767.40–769.56 m. Two samples of YC01 and YC02 were retrieved at 769.0 and 769.3 m depths, respectively (Figure 3 and Figure S2 in Supporting Information S1; Table 1).

The syn-rift sediments in borehole ZK3 are 1,370.30 m thick and are underlain by Permian to Carboniferous strata. The available cores of syn-rift sediments are distributed from 1,058.20 to 1,147.52 m, semi-consolidated fluvial and lacustrine sediments of alternating thin layers of pebbles, sand, and silt. Six samples were collected from ZK3 at depths of 1,060.8–1,065.4 m (WQ01 and WQ02), 1,115.8 m (WQ04), 1,143.8–1,144.3 m (WQ08, WQ05, and WQ09), which are all semi-consolidated medium-coarse sand with fine pebbles (Figure 3 and Figure S3 in Supporting Information S1; Table 1). Notably, no volcanic rocks or debris were observed in these boreholes, further corroborating the magma-poor nature of the SRS.

SU ET AL. 5 of 22

L Elev. 807 m

178

C Flev 965 m

185.22

G Elev. 783 m

145.41

M Elev. 834 m

110.00

605.02

670.19 685.89

0 m 16.54 34.77

0 m 12.13

2 52.64 62.71

D Flev 973 m

10.06 14.49

0 m 6.80 33.68

80.51

209.80

H Elev. 1002 m

- 29.86

N Elev. 958 m

654 40

718.50 735.22

114.60

559 10

Previous boreholes

A Elev. 1252 m B Elev. 1037 m

164.20

279.25

K Elev. 779 m

685

1281.65

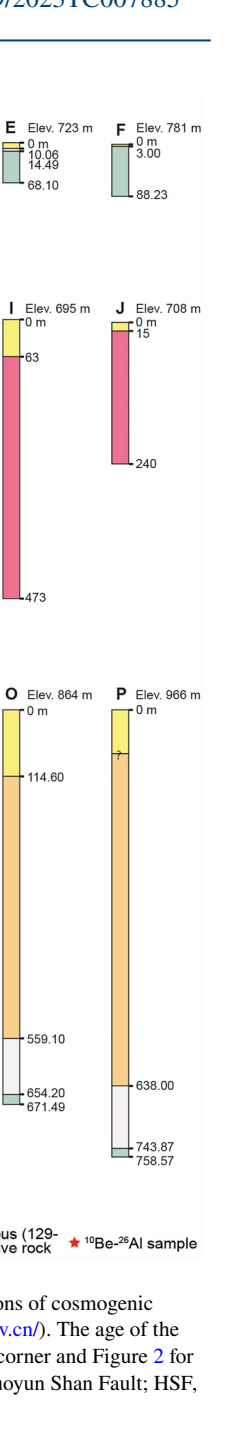


Figure 3. Simplified stratigraphic columns derived from the new and previous boreholes with locations of cosmogenic samples. Previous boreholes are collected from the China Geological Survey (https://geocloud.cgs.gov.cn/). The age of the Early Cretaceous intrusive rocks is based on Yang et al. (2017). See the index map in the bottom left corner and Figure 2 for borehole locations. The blue line denotes the seismic reflections profile A-A'. Abbreviations: LSF, Luoyun Shan Fault; HSF, Huo Shan Piedmont Fault.

1308.82

Carboniferous Ordovician

3.1.2. Sample Analysis

Late Miocene-Quaternary

New boreholes

7K2 Flev 447 m

7K3 Flev 445 m

ZK1 Elev. 479 m 0 m Depth

440.90

619.39

1277.69 1339.01 1381.66 YC01 YC02 → 786.80

WOO

1413 95

• K

Triassic

WQ08 WQ05 WQ09

1370.30

Permiar

100 m

S03

All samples were prepared and analyzed at the Purdue Rare Isotope Measurement Laboratory (PRIME Lab), Purdue University. The samples were sieved, and the 250-500 µm size fractions were further processed through physical and chemical procedures to purify quartz. Beryllium (Be) and aluminum (Al) were extracted following procedures used by Granger et al. (2015). The ²⁶Al/²⁷Al and ¹⁰Be/⁹Be ratios were measured by accelerator mass spectrometry. The ²⁶Al and ¹⁰Be concentrations were derived from the measured ratios, ²⁷Al contents, and the ⁹Be spike with known concentration. See Text S1 in Supporting Information S1 for detailed experimental procedures.

We used a simple burial model to constrain the sediment burial age (Granger & Muzikar, 2001), considering that (a) the sediments to be dated were buried rapidly relative to the burial duration, (b) they were buried deep

SU ET AL. 6 of 22

1949194, 2023, 9, Downloaded from https://agupubs.onlinelibrary.wiley.com/doi/10.1029/2023TC007885 by Purdue University (West Lafayette), Wiley Online Library on [17/06/2024]. See the Terms

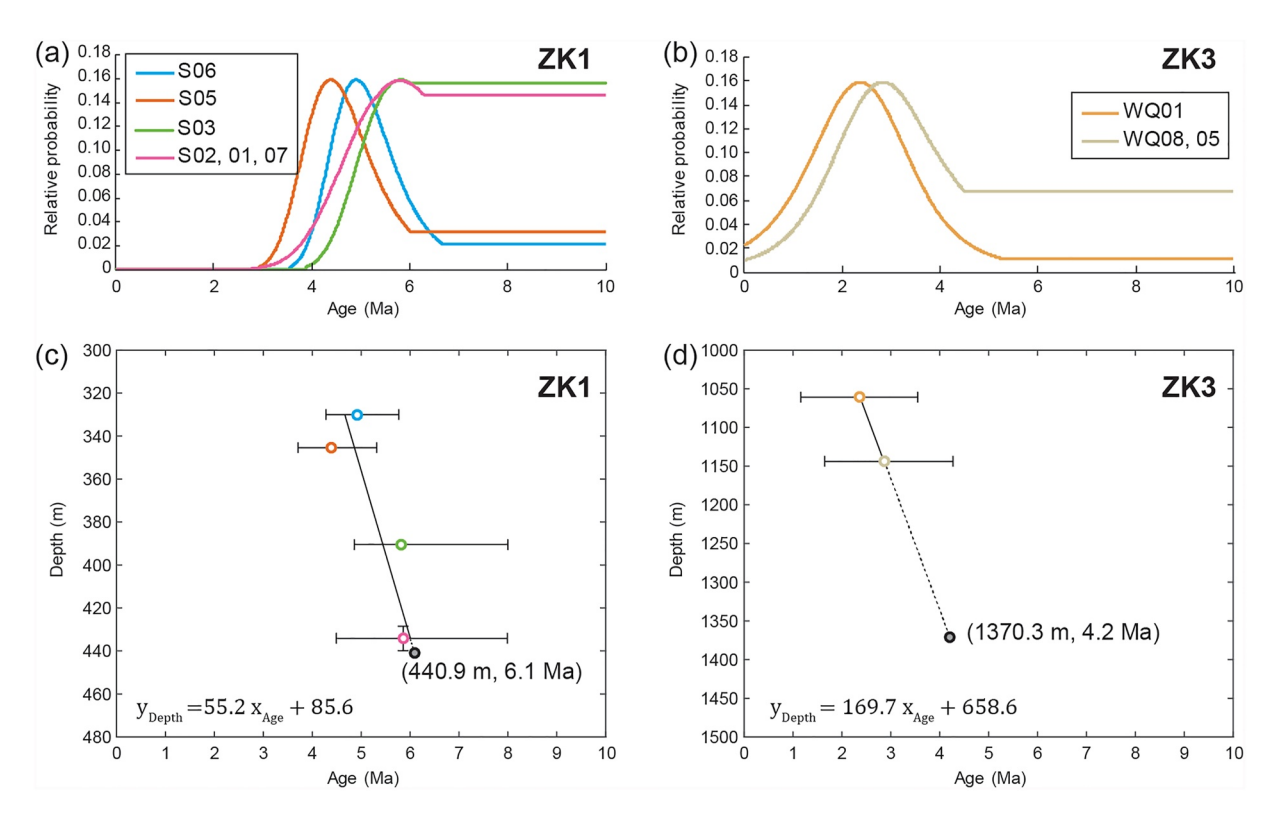


Figure 4. Analysis results of 26 Al/ 10 Be burial ages from ZK1 and ZK3. (a, b) Plots of probability density functions (pdfs) for the samples that have concentrations significantly above zero, showing the relative likelihood of the samples being a certain age. (c, d) Plots of 26 Al/ 10 Be burial ages against depths below the ground surface. Colored circles represent the most likely ages with horizontal uncertainty bars representing 1σ standard error. The ages with vertical uncertainty bars represent the depth range of the combined samples. Black circles represent estimated basal ages derived to first-order by linear extrapolation of the analyzed data.

enough (>30 m) to fully shield cosmic radiation, and (c) they were buried only once since the subsiding of the LB (SSB, 1988). Samples YC01 and YC02 from borehole ZK2 did not yield enough ²⁶Al and ¹⁰Be for burial age calculation (Table 1). These samples are likely old, but without knowledge of initial ²⁶Al and ¹⁰Be concentrations, we are unable to place constraints on the ages. The remaining samples had low but measurable ²⁶Al and ¹⁰Be concentrations, but many had ²⁶Al concentrations near the detection limits. For these samples, we can calculate a simple burial age. However, the uncertainty on the age is highly asymmetric, in some cases being unbounded on the high end. To express the uncertainty, we calculated probability density functions (pdfs) showing the relative likelihood that a given age is consistent with the measured concentrations (Figures 4a and 4b). The pdfs are normalized to peak height rather than area, because the ends of the distributions may be unconstrained. Where the burial age solution does not converge to a finite age, we took those pdfs and extended a line horizontally beyond the oldest finite solution (Figures 4a and 4b). Although, in some cases, the maximum age is constrained by the measured ¹⁰Be concentration, the pdfs are based on the joint solution of ²⁶Al and ¹⁰Be and are shown as unconstrained. For the source area production rates before burial, we used a ¹⁰Be production rate of 9 at g⁻¹ yr⁻¹ based on the present-day production rate at 36°N, 111°E and elevation 1,500 m and the scaling model of Lifton et al. (2014) and a ²⁶Al/¹⁰Be production rate ratio of 6.8. We neglected the production by muons due to the extremely deep burial depths. See Text S1 in Supporting Information S1 for detailed calculations.

3.2. Quantitative Structural Modeling

3.2.1. Multiple Constraints and Seismic Interpretation

The curvature of a normal fault at depth usually prevents an accurate estimation of basin extension from surface observation of the dip and throw of the fault (McKenzie, 1978). To overcome this issue, we used multiple constraints to define the geometry of the LB, including surface geology, boreholes, and a deep seismic-reflection profile across the LB. The near-surface structural cross-section along the seismic-reflection profile was defined by integrating the field-based structural mapping and analysis of geological maps (SPGEB, 1975–1978). Since

SU ET AL. 7 of 22

many strata are not exposed, the ZK3 and 16 previous boreholes adjacent to the seismic line were used as the near-surface geological constraints. Because these boreholes have spatial coordinates (i.e., longitude, latitude, and elevation) and the corresponding stratigraphic columns record the strata depths, each stratum's spatial coordinates can be obtained (Figures 2 and 3). The fault throw can be thus constrained by comparing the elevation of a stratum from two sides of a fault.

The deep seismic-reflection profile was obtained by Z. Li et al. (2014). The new borehole ZK3 is located on the profile (Figure 2). We re-interpreted the seismic profile with the surface cross-section and the borehole data (Figure 5). Generalized reflectors were interpreted based on the regional geology and previous studies (Z. Li et al., 2014; SPGEB, 1975–1978). Strong, continuous reflectors that are horizontal or low-angle dipping are interpreted as marker beds or structures. Bright spots are interpreted as intrusive rocks. The "smile" features and high-angle intersecting reflections are regarded as artifacts introduced in seismic processing (Zhou, 2014). The surface geological constraints and borehole data were tied to the seismic profile and presented without vertical exaggeration during the analysis. Because the stratigraphic markers used for structural modeling are within 2 s (two-way travel time, TWT), we used the crustal average *P*-wave velocity of \sim 3 km/s within 2 s (Z. Li et al., 2014) to estimate the depth (Figure 6). The tops of the Permian and Carboniferous in the ZK3 are thus estimated to be at depths of \sim 1.35 km (\sim 0.9 s TWT) and 1.8 km (\sim 1.2 s TWT) on the seismic profile (Figure 6), which are roughly consistent with the depths of 1,370.30 and 1,710.03 m observed (Figure 3), indicating the velocity used for time-depth conversion is reasonable.

3.2.2. Structural Modeling

To quantitatively obtain the geometry and the total amount of extension of the LB, we used the structural modeling software StructureSolver® to reproduce these observed constraints (Eichelberger et al., 2015). This forward modeling approach combines a fault segment with theoretical stratigraphic horizons on either side of the fault and further constructs a 2-D structural model based on the rollover geometrical relationship (Xiao & Suppe, 1992). The model contains quantitative information on fault geometry, deformed stratigraphic shapes, and fault displacement. The geometry of modeled stratigraphic surfaces is based on the extensional fault-bend folding theory (Xiao & Suppe, 1992).

The modeled stratigraphic shapes depend on the stratigraphic depths in both hanging-wall and footwall, subsurface fault geometry and fault displacement, and the Coulomb shear direction (Xiao & Suppe, 1992). Based on the observed surface structure on the rift shoulders (refer to Section 4.2), we assume the pre-rift sedimentary strata in the study region are horizontal and were only deformed by rifting. The observed multiple constraints can define the pre-rift stratigraphic markers of the Permian, Carboniferous, and the top of the basement. In particular, the top Carboniferous can be well traced across the LB and its shoulders (Figure 6a). In our model, stratum depths in the hanging wall and footwall are based on these multiple constraints. The fault geometry near the surface is constrained by the fault dip of 80° at the surface (Figure 2). To yield the subsurface fault trajectory and fault displacement, we repeatedly adjusted the subsurface fault geometry to create a variety of possible fault morphologies and corresponding stratigraphic horizons, to reproduce the shapes and positions of these stratigraphic markers. The Coulomb shear direction (called shear angle in StructureSolver®) is the angle of the shear axis with respect to undeformed bedding. Here, we assume the Coulomb shear direction to be 67° from horizontal according to Xiao and Suppe (1992). Trishear deformation and compaction were not considered in the modeling.

4. Results

4.1. Deposition Age

Nine samples from ZK1 (S01, 02, 03, 05, 06, 07) and ZK3 (WQ01, 05, 08) were used in concert with each other to constrain the deposition ages of the cores (Figure 4; Table 1). All samples show low concentrations of 26 Al and 10 Be, and many yield ages near the upper limit of burial dating with these nuclides. The upper two samples of S06 and S05 from ZK1 have robust age constraints of $4.91^{+0.86/-0.63}$ Ma and $4.39^{+0.93/-0.68}$ Ma, respectively, overlapping within measurement uncertainty. The deeper sample S03 has a very low 26 Al concentration, within 2σ of zero, which means that the 26 Al/ 10 Be burial age is a minimum and unconstrained on the high end. Its inferred burial age is $5.82^{+inf/-0.96}$ Ma. Although the modeled age using the 26 Al- 10 Be pair is not well constrained, the 10 Be concentration in this sample is well above detection limits. This suggests that the sample is younger than 8 Ma, or there would be little remaining 10 Be due to radioactive decay. As a first-order approximation, the 10 Be

SU ET AL. 8 of 22

19449 194, 2023, 9, Downloaded from https://agupubs.onlinelibrary.wiley.com/doi/10.1029/2023TC007885 by Pudue University (West Lafayette), Wiley Online Library on [17/06/2024]. See the Terms and Conditions (https://onlinelibrary.wiley.com/terms

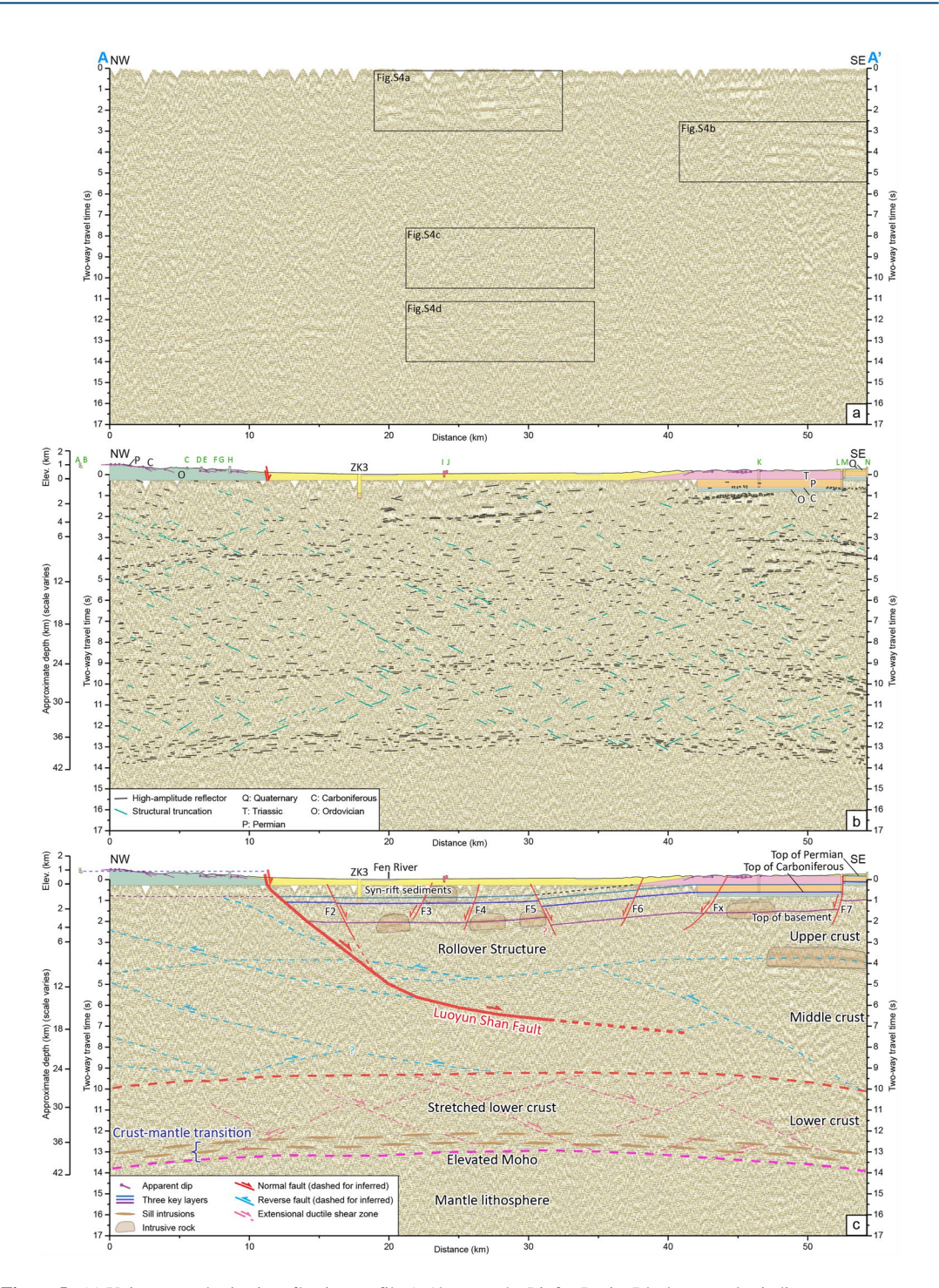


Figure 5. (a) Uninterpreted seismic-reflection profile A-A' across the Linfen Basin. Black rectangles indicate areas magnified in Figure S4 in Supporting Information S1 showing representative reflections. The original seismic image can be found in the Data Availability Statement section. (b) Simplified composite lines of the high-amplitude reflectors and structural truncations in the seismic profile. The surface geological constraints of the geological cross-section, boreholes, and dips are tied to the seismic section. (c) Preliminary interpretation of the seismic-reflection profile based on seismic-reflection characters, the multiple surface geological constraints, and the regional geological setting. The original seismic data, intrabasin faults, and crustal velocity used to determine the depth scale are from Z. Li et al. (2014). See Figure 2 for locations.

concentration in sample S03 is about half that of sample S06. If the two samples were originally buried with similar 10 Be concentrations, one could estimate that S03 is approximately one 10 Be half-life (i.e., 1.4 Myr) older, placing it at \sim 6.3 Ma. It is unlikely that the actual age of this sample exceeds 8 Ma.

SU ET AL. 9 of 22

1949194, 2023, 9, Downloaded from https://agupubts.onlinelibrary.wiley.com/doi/10.1029/2023TC007885 by Purdue University (West Lafayette), Wiley Online Library on [17/06/2024]. See the Terms and Co

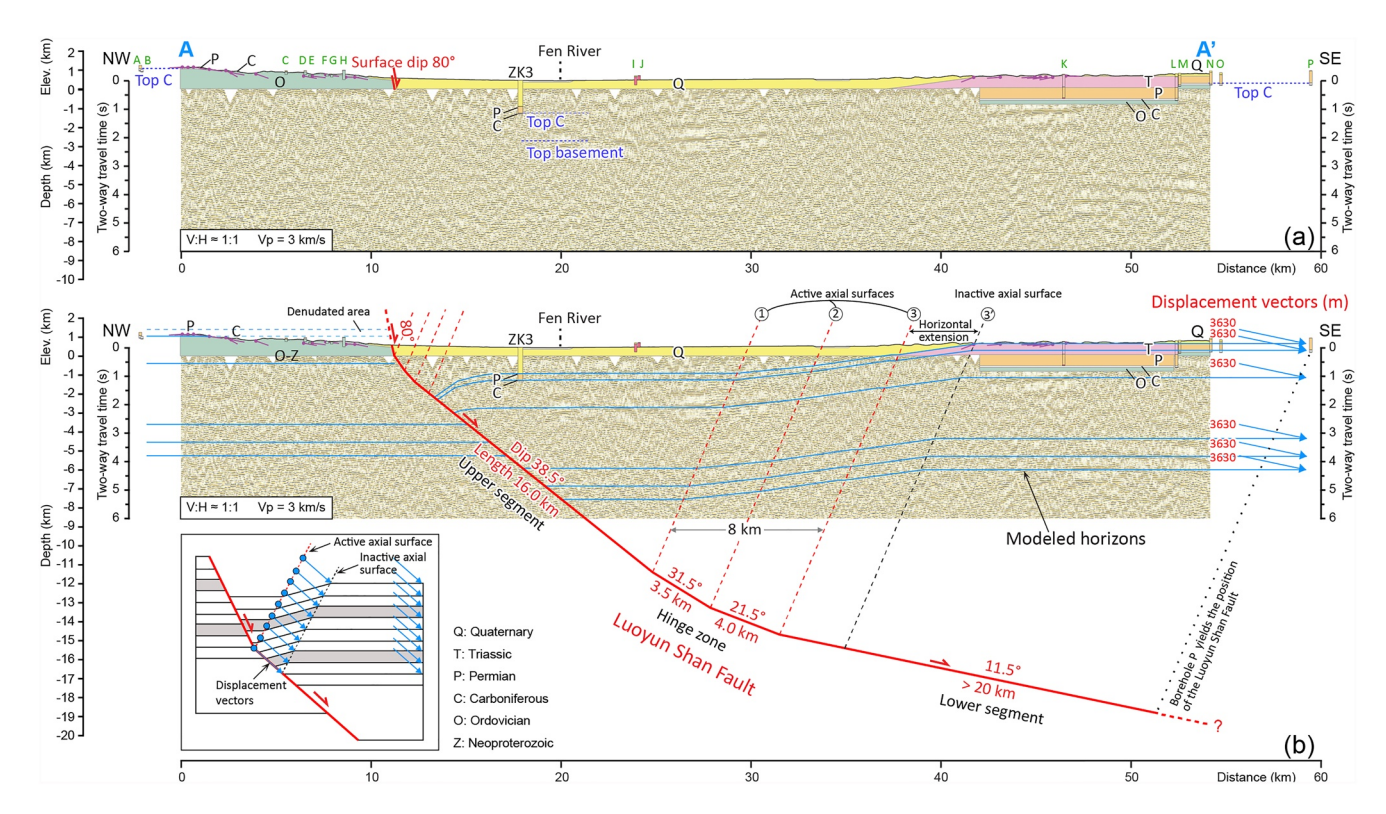


Figure 6. (a) Uninterpreted seismic-reflection profile A-A' marked with geological constraints of the surface geological cross-section, boreholes, and dip ticks. Only the upper part (0-6 s TWT) is shown. A crustal average P-wave velocity of ~ 3 km/s within 2 s TWT (Z. Li et al., 2014) is used for time-depth conversion. (b) Structural model of the Linfen Basin constrained by quantitative structural modeling of the multiple constraints. The black dashed line 3' denotes the corresponding inactive axial surface of the active axial surface 3. The dotted black line demonstrates the position of the minimum length and depth of the lower segment. The inset figure shows the rollover structural model (Xiao & Suppe, 1992) that was implemented in the StructureSolver® as the inclined-shear algorithm. Dip ticks show apparent dips with no vertical exaggeration. See Figure 2 for locations.

Samples S02, 01, and 07 yield very low concentrations of 26 Al and 10 Be. Because these samples were collected near each other, the results were averaged to reduce the uncertainty, yielding a minimum age constraint with a burial age of $5.86^{+inf/-1.37}$ Ma. Similarly, in sample S03, the 26 Al concentration is near detection limits, so the age is unconstrained on the high end. The 10 Be concentration for two of the three samples is above detection limits, suggesting again that these samples are younger than about 8 Ma. The 10 Be concentration of these deeper samples is lower than in sample S03, consistent with them being older but less than \sim 8 Ma.

Sample WQ01 and the average of samples WQ08 and WQ05 from ZK3 yield reliable ages of 2.37^{+1.18/-1.21} and 2.86^{+1.41/-1.21} Ma, respectively. The other five samples (YC01, 02, WQ02, 04, 09) were excluded as their cosmogenic nuclide concentrations are below detection limits, that is, too low to give the true age of the deposit.

4.2. Surface Structure

Within the LB, the depth of syn-rift sediments at the ZK3 is 1,370.3 m (Figures 3, 5 and 6). On the western shoulder of the basin, the dip angles of the exposed Permian-Ordovician strata are less than 10° and the boreholes also suggest the strata are nearly flat (Figures 2, 5, and 6), indicating the Yanshanian orogeny caused limited deformation to the observed strata in the study area. Comparing the top of the Carboniferous from boreholes A, B, D, and H in the footwall of the LSF with that from borehole ZK3 in the hanging wall, the total throw of the LSF near the cross-section is estimated to be $2,281 \pm 62$ m (Figures 2, 3, 5, and 6).

On the eastern shoulder of the basin, boreholes K and L reveal Triassic-Ordovician strata between 46 and 53 km on the section, and boreholes M, N, O, and P show Permian-Ordovician strata between 53 and 60 km, all of which suggest largely flat strata on both sides of the F7 fault. The total throw of this fault is 793 ± 43 m as indicated by correlating the top of the Carboniferous (Figures 3, 5, and 6). Note that the topography has no vertical offset, indicating that the F7 fault does not control the rift configuration (Figures 2, 5, and 6).

SU ET AL. 10 of 22

4.3. Deep Structure

Tectonics

The original seismic reflection profile across the LB (Z. Li et al., 2014) and our reinterpretation are shown in Figure 5 and Figure S4 in Supporting Information S1. The densely distributed, massive stratified reflectors at 12.5–14 s depth can be interpreted as a series of sill intrusions at the crust-mantle transition (e.g., Thybo & Artemieva, 2013; Thybo et al., 2000). The bottom of this transition is interpreted as the Moho (Z. Li et al., 2014). The crust mainly consists of three layers, that is, the upper, middle, and lower crust. The bottoms of these layers are at 4–5, 9–10, and 12.5–14 s, respectively. The lower crust is elevated under the axis of the rift basin and the deformation zone is wider than the basin domain at the surface. It appears that truncations are widely distributed in the middle crust. Beneath the western shoulder of the rift, we interpret that the faults in the upper crust do not cut across the lower crust. The intrusive rocks are mainly located around the top of the basement and sporadically distributed around the top of the middle crust (Figure 5).

The LB is characterized by a typical rollover geometry based on the deformed pre-rift stratigraphic markers (i.e., Permian, Carboniferous, and top of the basement) revealed by the seismic profile and the geological constraints (Figure 5). The top of the basement is characterized as continuous, high-amplitude seismic reflectors, which are distinct at ~2 s at ~20–32 km on the seismic profile (Figure 5b). Reflectors become inclined between ~32 and 42 km, dipping to the northwest. The imaged horizons of syn-rift sedimentary rocks at 15–32 km are nearly flat on the profile, and further southeast they become gently tilted toward the basin. The sedimentary rocks progressively become thinner toward the eastern flank of the basin, suggesting the basin has been growing since the onset of sedimentation (Figures 5b and 5c). The seismic image shows relatively continuous reflectors of variable amplitude within the sedimentary cover. As seismic data do not image obvious offsets in the syn-rift sediments at the F5 fault (Z. Li et al., 2014), we infer the basin bottom across F5 is also continuous as it is across the F7 fault (Figure 5c). Several relatively continuous reflectors within the basement can be imaged at ~3.5–5.0 s, and we interpret the deepest one as the bottom of the upper crust (Z. Li et al., 2014). Based on the overall rollover geometry of the sedimentary strata and the structural truncations on the seismic image (Figure 5b), we infer the LSF as a listric normal fault, which extends from the surface and soles into a low-angle detachment in the middle crust (Figure 5c).

4.4. Structural Model

The border LSF primarily controls the rift basin, and the intrabasin faults accommodated a very small portion of the extensional strains (Figure 5c) (Z. Li et al., 2014). Therefore, following Xiao and Suppe (1992), we neglected these intrabasin faults in the forward modeling. The surface geological constraints were used beyond the sub-structure between the F5 and F7 faults. Boreholes I and J indicated a structural high within the basin consisting of igneous rocks, which we interpreted as a residual relief related to pre-rift tectonic phases (Figure 6a). We constructed a 2D structural model of the LB (Figure 6b). Although this simplified geometric model neglects the heterogeneities of natural rock properties that will affect the Coulomb shear direction (Xiao & Suppe, 1992), the modeled horizons fit well with the observed stratigraphic markers of the Permian, Carboniferous, and the top of the basement (Figure 6b), indicating that the forward kinematic model is viable.

The LSF mainly consists of two planar segments connected by a concave-upward hinge zone (Figure 6b). The upper segment has a higher angle (38.5°), extending from the near-surface to \sim 12 km depth with a length of \sim 16.0 km. The dip angle abruptly increases to \sim 80° near the surface. The lower segment with a low angle (11.5°) extends from \sim 15 km to more than 19 km depth with a length of more than 20 km. The available constraints do not define the position of the downward termination. The hinge zone of the LSF is at a depth of 12–15 km with a horizontal width of \sim 8 km. The model also demonstrates that the current footwall experienced denudation, and the denuded thickness ranges from 0.3 to 0.8 km. The total extensional displacement of the LB along the profile is \sim 3.6 km, and the value of the corresponding horizontal displacement is nearly the same by projecting this displacement vector onto the horizontal (Figure 6b).

5. Discussion

5.1. Timing and Extension Rate of the Linfen Basin

We use the most probable ages without considering the data errors, recognizing that the values have a large degree of uncertainty. Regressing the sample ages by their depths can constrain the sediment accumulation rate during the age span of these samples. At the location of borehole ZK1 in the southern LB (Figure 2), the mean

SU ET AL. 11 of 22

sediment accumulation rate is ca. 55 m/Myr at depths from 330 to 434.2 ± 5.7 m (Figure 4c; Table 1). By linear extrapolation of the observed sample ages and depths downward, the basal age at 440.9 m depth at borehole ZK1 is estimated to be \sim 6.1 Ma (Figure 4c). At the location of borehole ZK3 in the northern basin (Figure 2), samples WQ01, 05, and 08 are much deeper than the samples in borehole ZK1. Still, they are much younger, indicating a faster sediment accumulation rate. The mean sediment accumulation rate is ca. 170 m/Myr from depths between 1,060.8 m and 1,144.0 \pm 0.1 m at ZK3 (Figure 4d; Table 1). By linear extrapolation downward to 1,370.3 m depth at this sediment accumulation rate, we estimate a basal age of \sim 4.2 Ma at ZK3 (Figure 4d).

Combined with the total extension of \sim 3.6 km and the timing of initial syn-rift sedimentation of \sim 4.2 Ma along the section across the ZK3 in the northern basin, the mean extension rate is yielded to be \sim 0.9 km/Myr. The average strain is \sim 13.1%, calculated by dividing the accumulated extension (\sim 3.6 km) by the width of the zone before the extension (31.0 – 3.6 = 27.4 km). The corresponding average strain rate is \sim 1 × 10⁻¹⁵ s⁻¹ calculated by dividing the average strain (\sim 13.1%) by the extension duration (\sim 4.2 Ma). Considering our obtained deposition rate at ZK1 in the southern basin (\sim 55 m/Myr) is smaller than that at ZK3 in the northern basin (\sim 170 m/Myr), we infer the long-term mean extension rate of the southern basin is smaller than the northern portion of the LB. The total fault throw of 2,281 \pm 62 m near ZK3 likely represents the maximum fault throw along the LSF considering the basin depths from ZK1 to ZK3 increasing northward (Figures 2 and 3). The corresponding mean throw rate is 0.54 \pm 0.01 km/Myr by dividing the total throw (2,281 \pm 62 m, refer to Section 4.2) by the age (\sim 4.2 Ma).

The observed long-term extension rate of \sim 0.9 km/Myr across the LB is consistent with the present dip-slip rate of 1.1 \pm 0.3 mm/yr obtained by precise leveling measurements (recorded from 1970 to 2014) across the southern portion of the LSF (Hao et al., 2016). GPS data have not yielded a valid extension rate of the LB (e.g., 0.2 \pm 0.8 mm/yr, B. Zhao et al., 2017), most likely because the slow extension rate is below its measurement limit. The similar low rates from both long-term and short-term observations imply that the extension across the LB of the SRS has been constantly slow in the order of 1 mm/yr since the late Miocene.

5.2. Late Miocene Rifting Process of the SRS

Although there are large uncertainties in the basal age estimates, the sample ages at ZK3 are consistently younger than those from ZK1, despite being deeper, which suggests that subsidence at ZK3 occurred later but faster. The basal age-depth associations at ZK1 (~6.1 Ma, ~440.9 m) and ZK3 (~4.2 Ma, ~1,370.3 m) present that the syn-rift sediments are distinctly thicker at ZK3 but initiated ~2 Myr later. This suggests that the onset of deposition is diachronous in the LB with the southern part initiated earlier. Moreover, the differential basin depths are not controlled by the differential onset of faulting (considering more subsidence at the younger site). Still, they may be mainly related to the differential throw rates along the LSF.

Comparing the age constraints of the LB with that of other basins of the SRS enables us to understand the rifting process of this *en-échelon* rift system (Figure 7). Our age constraints of \sim 6.1 and \sim 4.2 Ma in the southern and northern portions of the LB, respectively, suggest diachronous rifting propagating northward within the basin. Southward, this late Miocene episode is constrained to be \sim 8 Ma by thermochronology of the latest rapid cooling in the Zhongtiao Shan (Su et al., 2021) and \sim 7 Ma by the magnetostratigraphy of the latest unconformity in the Sanmenxia Basin (X. Chen et al., 2021) (Figure 7). Further southward in the Qinling range, the timing is constrained to be \sim 10 Ma by thermochronology (Heberer et al., 2014; J. Liu et al., 2013) and \sim 9.5 Ma by magnetostratigraphy (Z. Wang et al., 2012). Collectively, these observations indicate that during the late Miocene tectonic evolution, the rifting propagated northward from the WB at \sim 10 Ma, to the Yuncheng Basin at \sim 7–8 Ma, and to LB at \sim 6-4 Ma (Figure 7). Although the exact timing of the northward propagation process remains poorly constrained considering the uncertainties of these age data, we argue that the northward propagation trend is real because our ages in the LB cannot exceed 8 Ma, otherwise there would be no remaining detectable ¹⁰Be. Although the propagation process from the Taiyuan Basin (TB) to DB cannot be interpreted confidently due to sparse age constraints, it seems the nucleation of the rift segments near the YB, the TB, and the DB are isolated with similar initial timing based on the comparable ages observed and the discrete rift morphology (Figure 7).

5.3. Basin-Scale Non-Rigid Transtensional Bookshelf Faulting Model

The basal age of \sim 6.1 Ma of the LB is consistent with the timing of the late Miocene tectonic episode widely observed in North China (Figure 7) (Su et al., 2021, and the references therein). Although it has been widely accepted that the kinematics of the SRS is characterized by right-lateral transtensional slip and North China

SU ET AL. 12 of 22

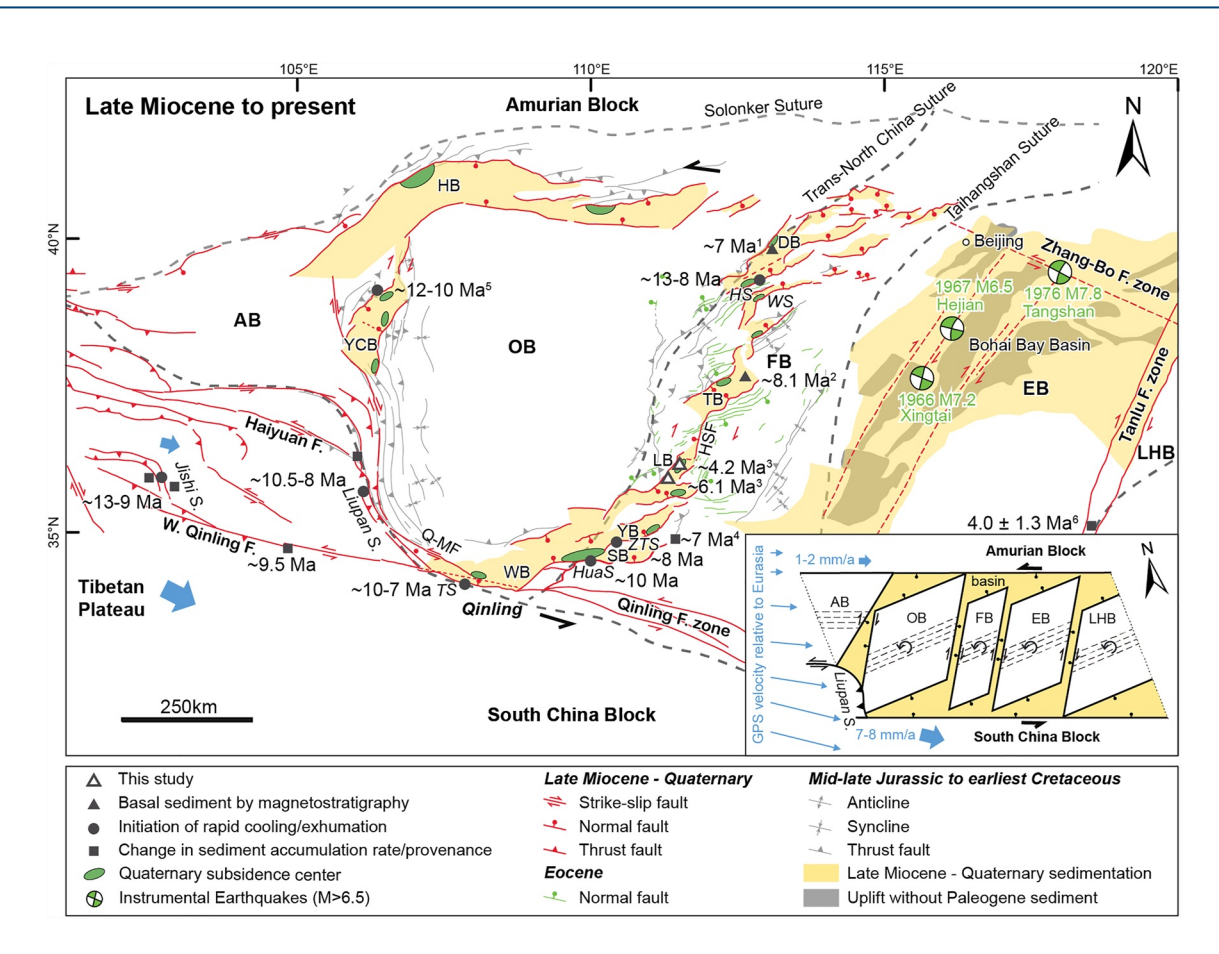
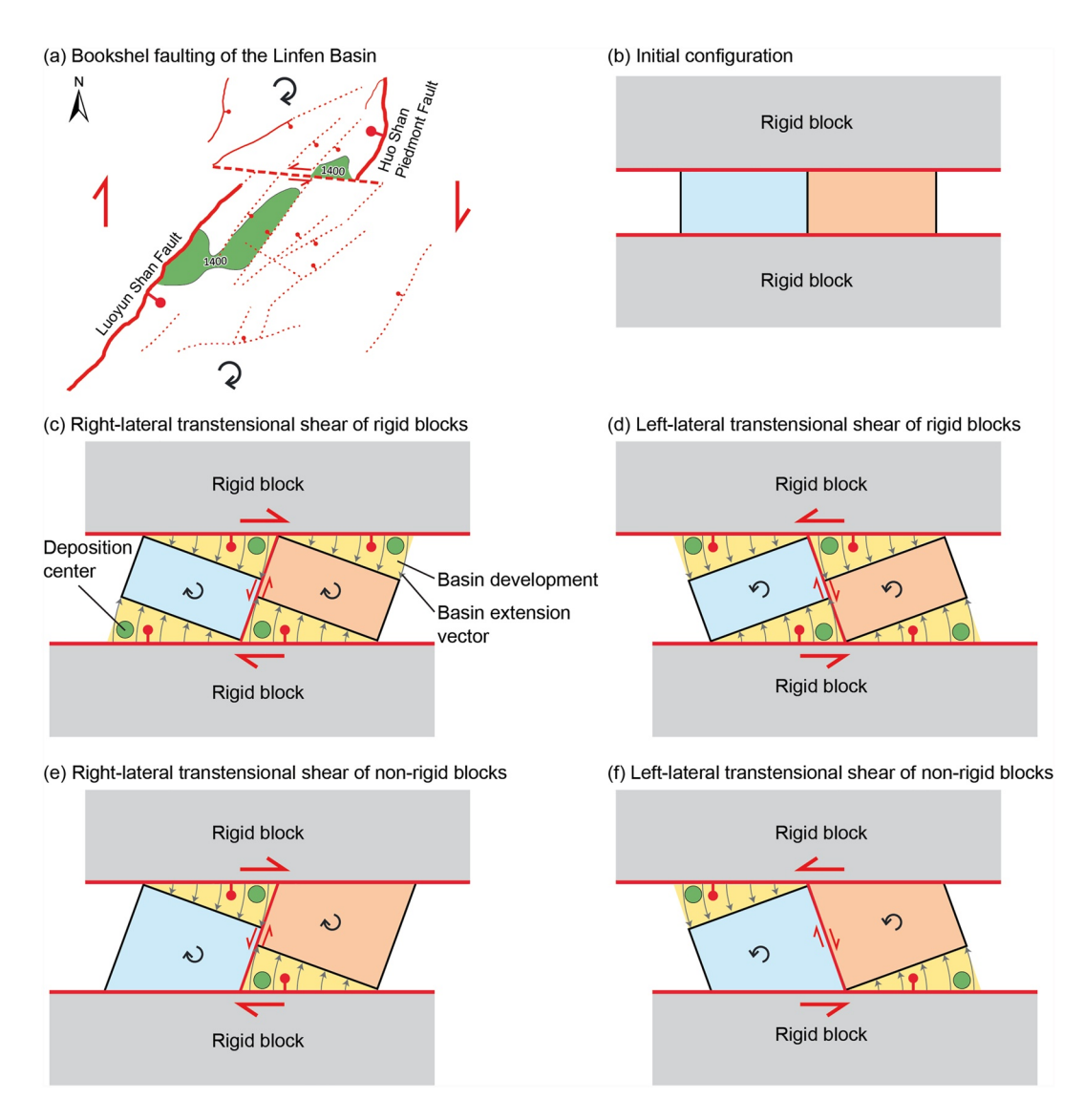


Figure 7. Spatial distribution of rift basins and structures in North China since the late Miocene (modified after Su et al., 2021). Quaternary subsidence centers are from SSB (1988) constrained by seismic reflection profiles. Inset is the craton-scale rigid transtensional bookshelf faulting model of North China, in map view. Continued India-Eurasia collision induced differential eastward motion among the Amurian, North China, and South China Blocks, leading to counterclockwise, bookshelf-style rotation of rigid subblocks in North China. The new data sources are (1) Bi et al. (2022), (2) R. Wei et al. (2022), (3) This study, (4) X. Chen et al., 2021, (5) J. Liu et al. (2010), and (6) Shu et al. (2023). Abbreviations: DB, Datong Basin; HB, Hetao Basin; LB, Linfen Basin; SB, Sanmenxia Basin; TB, Taiyuan Basin; WB, Weihe Basin; YB, Yuncheng Basin; YCB, Yinchuan Basin; TS, Taibai Shan; HuaS, Hua Shan; HS, Heng Shan; WS, Wutai Shan; Q-MF, Qishan-Mazhao Fault; HSF, Huoshan Piedmont Fault; AB, Alxa Block; OB, Ordos Block; FB, Fuping Block; EB, Eastern Block of the NCC; LHB, Ludong-Huanghai Block.

is characterized by counterclockwise, bookshelf-style rotation of rigid subblocks during this tectonic episode (here we name it the craton-scale rigid transtensional bookshelf faulting model, see inset of Figure 7) (e.g., Su et al., 2021; X. Xu & Ma, 1992), there remains a lack of evidence that directly reflects this kinematic pattern since the late Miocene. In addition, this model cannot account for some basin-scale kinematic observations. For example, this model requires the N-trending Huoshan Piedmont Fault to be a right-lateral strike-slip fault (X. Xu et al., 1993). However, fault striation observations of 20 groups from 10 sites along the fault confirm that this is a normal fault with a negligible oblique-slip component (Y. Xu et al., 2018).

The rotation patterns of the LB and other circum-Ordos basins provide new evidence of North China's craton-scale rigid transtensional bookshelf faulting model since the late Miocene. The depths of the late Miocene LB increase northward, that is, 440.9 m at ZK1, 786.8 m at ZK2, and 1,370.3 m at ZK3 from south to north (Figures 2 and 3). If one assumes the LSF has similar geometries along its strike at depth, we could infer that basin extension increases northward, considering that basin depths are mainly determined by the LSF throw (refer to Section 5.2). The northward increase of the basin extension further suggests the LB is in clockwise rotation under right-lateral transtensional shear (Figure 8a). Remarkably, the subsidence centers of many other circum-Ordos basins have concordant patterns of distributions (Figure 7) based on the Quaternary isopach maps available (SSB, 1988). Most of the basins have one primary subsidence center, close to one termination of the border fault rather than near its middle portion. For the basins on the east and west of the Ordos Block (OB), the subsidence centers are either near the northern portions of the western border faults or near the southern portions of the eastern border

SU ET AL. 13 of 22



19449194, 2023, 9, Downloaded from https://agupuls.onlinelibrary.wiley.com/doi/10.1029/2023TC007885 by Purdue University (West Lafayette), Wiley Online Library on [17/06/2024]. See the Terms and Conditions (thtps://onlinelibrary.wiley.

ons) on Wiley Online

Figure 8. Kinematic models of the asymmetric basin formation around the Ordos Block. (a) Bookshelf faulting model of the Linfen Basin. The faults and the basin sediment isopach of 1,400 m are simplified from Figure 2. (b) Original configuration of a transtensional bookshelf fault system with two bookshelf panels bounded by two rigid blocks on the bottom and top. (c) Basin development through basin-scale rigid transtensional bookshelf faulting model under right-lateral shear. (d) Basin development through basin-scale rigid transtensional bookshelf faulting model under left-lateral shear. (e) Basin development through basin-scale non-rigid transtensional bookshelf faulting model under right-lateral shear. (f) Basin development through basin-scale non-rigid transtensional bookshelf faulting model under left-lateral shear. Note that the width of the system changes as the basin extends.

faults (Figure 7), indicating clockwise rotation of the rift basins controlled by right-lateral transtensional shear (Figures 8b, 8c and 8e). For the basins on the north and south of the OB, the subsidence centers are either near the western portions of the northern border faults or near the eastern portions of the southern border faults (Figure 7), indicating counterclockwise rotation of the rift basins controlled by left-lateral transtensional shear (Figures 8b, 8d, and 8f). These shear patterns of the rift zones around the OB support the craton-scale rigid transtensional bookshelf faulting model (inset of Figure 7). Some basins (e.g., Yinchuan Basin) contain more than one bookshelf block that may rotate independently and form more than one subsidence center. The relatively small subsidence center within the WB in front of the Taibai Shan is likely an exception, which may be influenced by the left-lateral strike-slip faults of the West Qingling Fault and/or Qishan-Mazhao from outside of the basin (Figure 7).

We propose a basin-scale non-rigid transtensional bookshelf faulting model to account for the kinematic observations of rift basins around the OB (Figures 8e and 8f), following Zuza and Yin (2016). Taking the LB as

SU ET AL. 14 of 22

an example, its rotation pattern indicates a basin-scale bookshelf system, which mainly consists of two minor bookshelf blocks of the LB and the basin in front of the Huo Shan, and a transfer fault of the Hongtong-Subao Fault (Figures 2 and 8a). The rigid transtensional bookshelf faulting model requires two subsidence centers for one rotated bookshelf block (Figures 8c and 8d), while only one subsidence center may be formed through the non-rigid transtensional bookshelf faulting model (Figures 8e and 8f). Most circum-Ordos basins have one primary subsidence center (Figure 7), consistent with the non-rigid transtensional bookshelf faulting model (Figures 8e and 8f). This may imply that the rotated bookshelf blocks within the basins are non-rigid, and the potential subsidence regions were accommodated by distributed extensional deformation (Figures 8e and 8f) (e.g., Cheng et al., 2015; Zuza & Yin, 2016). The observed differential timing of the basal sedimentation of the LB also suggests that the rotated blocks are non-rigid. Moreover, no matter whether a rotated bookshelf block is rigid or non-rigid, the basin extension vectors in the models predict that the basin border faults are mainly normal (Figures 8c-8f), which can well explain the widely observed normal sense of the basin border faults around the OB formed under lateral shear, including the N-trending Huoshan Piedmont Fault (Figure 7) (SSB, 1988; Y. Xu et al., 2018).

5.4. Roles of Magmatism, Pre-Existing Structures, and Extension Rate

We further investigate the roles of magmatism, pre-existing structures, and extension rate in the evolution of the magma-poor SRS. The lower crust of the LB is characterized by high-velocity anomalies, high conductivity, positive radial anisotropy ($V_{\rm sv} < V_{\rm sh}$), and strong seismic reflectivity (Figure 5) (e.g., Dou et al., 2021; Z. Li et al., 2014; Ling et al., 2017, Y. Yin et al., 2017). Across the basin, the crust has a distinctly high V_p/V_s ratio of >1.85 (Ling et al., 2017; Z. Wei et al., 2011). These observations indicate mafic sill intrusions in the lower crust (Thybo & Artemieva, 2013) and the intrusions must have cooled to the ambient temperature (Y. Liu et al., 2021) (Figure 9). The similar degree of up-warping between sill intrusions in the lower crust and the Moho suggests the intrusions formed before rifting and deformed afterward (Figure 9). Considering that the exposed intrusive rocks in the LB were emplaced at ~129–125 Ma (Figure 2) (Yang et al., 2017), coeval with the extensive magmatic intrusion that occurred in the Early Cretaceous (~135–108 Ma) in the SRS region (Z. Ren et al., 2020), we infer that the mafic intrusions in the lower crust and at the Moho were also emplaced in this period, that is, long before the late Miocene rifting. Besides the inconsistent timing of magmatism and rifting, the cooled mafic intrusions could strengthen the lower crust, both of which preclude the magma-poor rifting model that suggests partial melts hiding at depth weaken the lithosphere and reduce the force required for rifting (e.g., Buck, 2004; Muirhead et al., 2016).

The SRS lies on the Trans-North China Orogen, which contains numerous pre-existing (pre-rift) structures (e.g., fabrics, foliations, and shear zones) as that observed on the seismic profile (Figure 5) (B. Zhang et al., 2021). These pre-existing fractures would form mechanically weak zones susceptible to reactivation during the subsequent tectonic evolution (e.g., Corti et al., 2011; Dunbar & Sawyer, 1988; Manatschal et al., 2021; Morley et al., 2004). By comparing the structural distribution of the SRS with that of the pre-rift structures in the SRS region, for example, normal faults formed in the Eocene, fold-and-thrusts formed during Middle-Late Jurassic to earliest Cretaceous (Yanshanian orogeny) and Paleoproterozoic (Trans-North China orogeny), and Paleoproterozoic sutures (Figure 7), Su et al. (2021) argued that these pre-existing structures play an important role in the evolution of the SRS. This argument is bolstered by the similar orientations between the modeled LSF (especially the upper segment) at depth and the structural truncations (some of them are regarded as reverse faults) interpreted on the seismic profile (Figures 5 and 9). Moreover, the calculated normal LSF dips less than 40° in the upper crust and even more gently in the middle crust (Figure 6b). Its dip is markedly smaller than 60° as predicted by Anderson's theory of faulting for isotropic rocks under coaxial stresses. This further indicates that the crust under the rift is anisotropic and the stress axes rotate around the weak zones (Morley, 2010), which can readily lead to tectonic reactivation (e.g., Corti et al., 2011; D'Agostino et al., 1998; Faccenna et al., 1995). In addition, the normal LSF is developed in the hanging wall of the Lishi thrust fault (Figure 2). We speculate that the LSF may sole into the Lishi Fault at depth or reactivate some segments during the late Miocene extension (Figures 2 and 10). Such a geometric relationship between the pre-existing thrust and the reactivated normal fault is common in many other magma-poor rifts such as the Rio Grande Rift (Y. Liu et al., 2019; A. Yin & Ingersoll, 1997). We thus ascribe the weakening of the cratonic lithosphere of the SRS to pre-existing structures.

The extension rate of the LB in the south-central SRS is very slow compared with other active continental rifts worldwide, 1–20 mm/yr (Tetreault & Buiter, 2018). The SRS with such a low extension rate and narrow

SU ET AL. 15 of 22

Tectonics



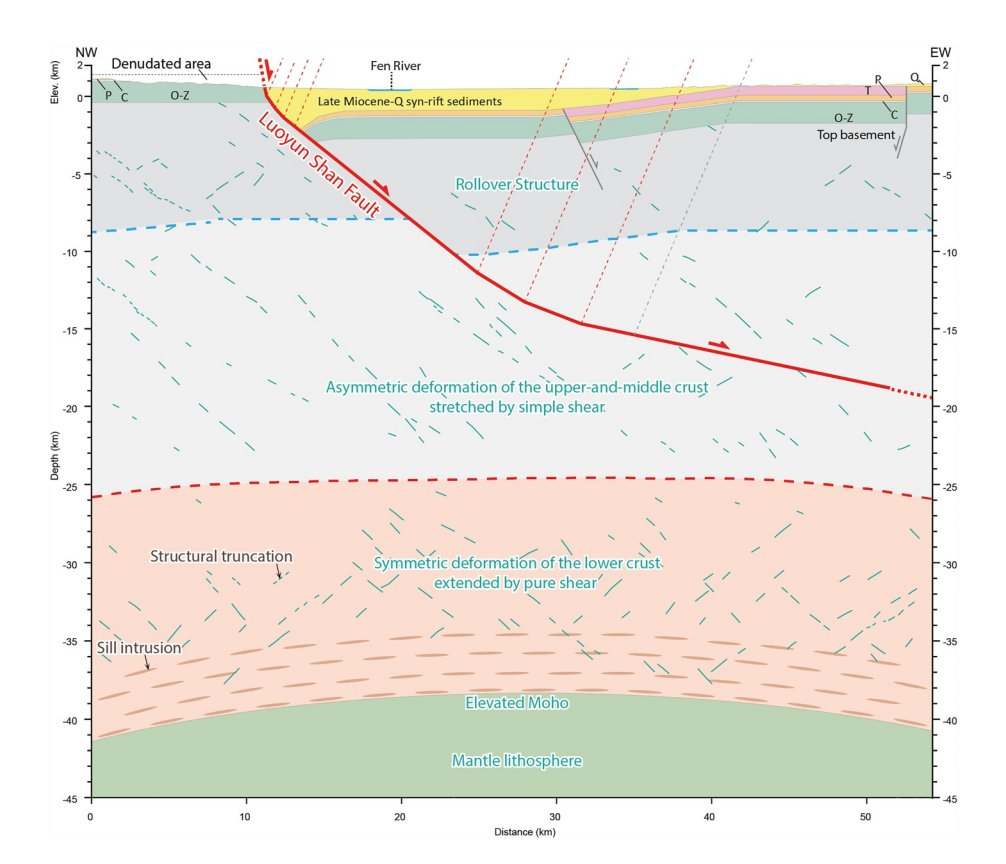


Figure 9. Simplified crustal structures of the Linfen Basin based on the seismic profile interpretation and quantitative structural modeling (Figures 5 and 6). Abbreviations: Q, Quaternary; P, Permian; C, Carboniferous; O, Ordovician; Z, Neoproterozoic.

morphology is consistent with narrow continental rifts such as the Baikal Rift and the Rio Grande Rift (Buck, 1991), indicating that it is possibly a general feature that narrow continental rifts have extension rates on the order of ~1 mm/yr. This feature is concordant with numerical simulation results, which suggest that the early stage of continental rifts is characterized by slow rifting (Ulvrova et al., 2019). Moreover, at such a slow extension rate, the conductive and convective heat diffusion is relatively large, giving the lower crust enough time to cool and regain its strength, which can also significantly prevent melt decompression (Gouiza & Naliboff, 2021; Pedersen & Ro, 1992; van Wijk & Cloetingh, 2002).

5.5. Lithospheric-Scale Magma-Poor Rifting Model of the Linfen Basin

We combine the crustal structure of the LB (Figure 9) with other findings regarding the basin's lithospheric configuration, to gain insights into the lithospheric-scale rifting of the magma-poor SRS (Figure 10). Although the extension of the LB in the upper-and-middle crust is asymmetric, the seismic profile demonstrates that the thinning of the lower crust is nearly symmetrically aligned with the basin (Figures 5, 9, and 10) (Z. Li et al., 2014). The sub-crustal mid-lithospheric discontinuity (MLD) is at 90–120 km, and the lithosphere-asthenosphere boundary (LAB) is at 190–200 km beneath the basin (L. Chen et al., 2014; S. Li et al., 2011). The up-warped Moho and MLD are localized under the basin axis (Figure 10), implying their configurations are associated with the rifting event since the late Miocene. The deformation zone of the Moho is more than three times wider than that observed at the surface, and the deformation degree of the sub-crustal lithosphere is even broader (e.g., Cai et al., 2021; S. Li et al., 2011) (Figure 10).

The ratio of the thickness outside the basin to the thickness beneath the basin (beta factor) shows the extent of thinning; the upper-and-middle crustal beta is $\sim 1.1 \ (\sim 27/\sim 25 \ \text{km})$. Assuming the MLD under the basin was flat before rifting, the beta of the sub-crustal lithosphere between the Moho and MLD is $\sim 1.1-1.5 \ (\sim 55-73/\sim 50 \ \text{km})$ (Figure 10). Therefore, the depth-dependent thinning suggests that the LB was not formed by a simple mechanical

SU ET AL. 16 of 22

19449194, 2023, 9, Downloaded from https://agupubs.onlinelibrary.wiley.com/doi/10.1029/2023TC007885 by Purdue University (West Lafayette), Wiley Online Library on [17/06/2024]. See the Terms and Conditions (https://online

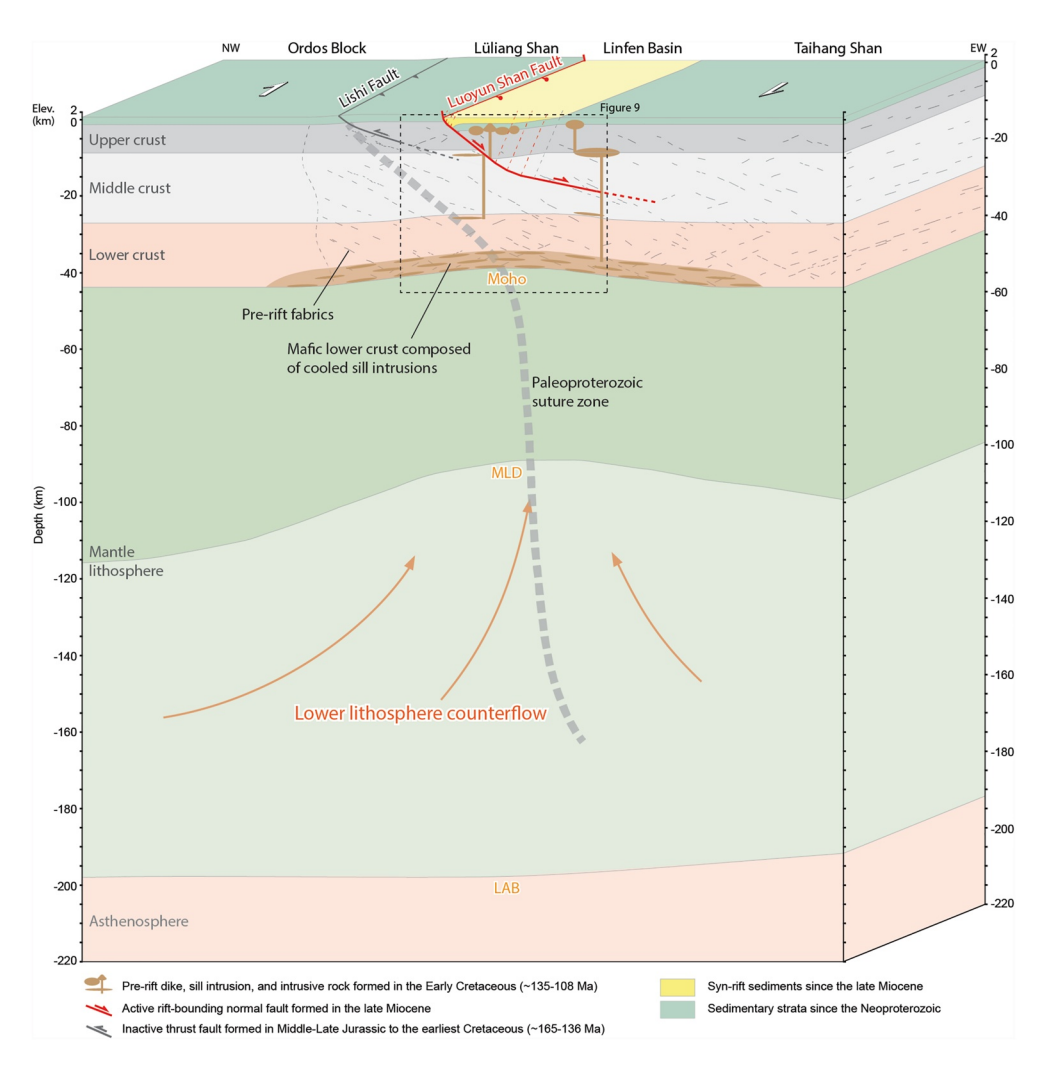


Figure 10. Conceptual lithospheric-scale rifting model in the Linfen Basin of the Shanxi Rift System summarizing the geological and geodynamic interpretations. The high-velocity anomalies in the lower crust (Dou et al., 2021; Ling et al., 2017) are interpreted as cooled sill-like intrusions. The Lüliang Shan in the research region is a monocline controlled by the Lishi Fault (B. Zhang et al., 2021). The pre-rift suture zone is inferred from G. Zhao et al. (2005). The mid-lithospheric discontinuity (MLD) and lithosphere-asthenosphere boundary (LAB) are modified from S. Li et al. (2011) and L. Chen et al. (2014). Note that the MLD was interpreted as LAB by S. Li et al. (2011) possibly due to the limitation of the wide-angle seismic refraction technique.

stretching (McKenzie, 1978). Notably, the LAB is nearly flat beneath the LB (Figure 10) (L. Chen et al., 2014). Suppose the Moho and MLD are initially nearly flat in the Linfen region. In that case, the current up-warped Moho and MLD above the flat LAB might be related to the upwelling materials from the lower lithospheric domain between the MLD and LAB. We suggest that the lower lithospheric counterflow proposed by Beaumont and Ings (2012) can explain all these observations, making it a viable mechanism for the SRS extension, at least in the LB region. It seems the upwelling of the lower lithospheric materials could absorb basal-lithospheric magma flow and may be more efficient than the asthenosphere upwelling; otherwise, the LAB would not have been that flat. This process would suppress magma production and contributes to the SRS's deficient magmatism. Moreover, the broad lower crustal extension would also reduce the concentration of the vertical mantle upwelling and is unfavorable for hot materials propagating to the shallow crust (Wilson et al., 2005).

Collectively, we propose a lithospheric-scale evolution model of the LB in the SRS (Figure 10). We infer the Paleoproterozoic sutures played the first-order role in the location of the SRS and other rifts in North China, as evidenced by many other continental rifts such as the Baikal Rift (e.g., Petit & Déverchère, 2006), the Rukwa Rift (Kolawole et al., 2021), and the Malawi Rift (e.g., Hopper et al., 2020). In response to the eastward extrusion of

SU ET AL. 17 of 22

the Tibetan Plateau since the late Miocene, the rift was reactivated under right-lateral transtensional shear (Su et al., 2021), which is a kind of oblique extension prone to facilitate rifting (Brune et al., 2012). The pre-existing fractures in the SRS region weakened the cratonic lithosphere and acted as exploitable weaknesses to influence the location, geometry, and evolution of the LSF during the rifting. The lower crust cooled and regained its strength at the slow extension rate of ~0.9 mm/yr. The lower lithospheric counterflow outpaced the asthenosphere upwelling and caused broad deformation zones in the lower crust and the sub-crustal lithosphere, all of which may have prevented magma from propagating to the shallow crust and resulted in the magma-poor nature of the basin. This study demonstrates that the inherited crustal weakness, low extension rate, and lithospheric counterflow all govern the LB evolution, providing an insight into the magma-poor rifting of the SRS, one of the magma-poorest continental rifts.

6. Conclusions

We have investigated the LB in the Shanxi Rift System (SRS) to evaluate continental magma-poor rifting. We have quantified the age, geometry, amount, and long-term rate of extension of the basin by integrating cosmogenic burial dating of 14 drill cores from three deep boreholes in the basin and quantitative structural modeling with multiple constraints, including the surface structural cross-section, 17 boreholes, and a seismic-reflection profile. Combined with previous observations of the region, this study leads to the following conclusions:

- 1. Cosmogenic 26 Al/ 10 Be burial dating yields six valid burial ages, ranging from $2.37^{+1.18/-1.21}$ to $5.86^{+inf/-1.37}$ Myr. The deposition time of the bottom sediments is estimated to be \sim 6.1 Ma at ZK1 in the southern basin and \sim 4.2 Ma at ZK3 in the northern basin, with diachronous rifting propagating northward.
- 2. Since 4.2 Ma along the research profile in the northern basin, the amount, mean rate, mean strain, and mean strain rate of the extension are \sim 3.6 km, \sim 0.9 km/Myr, \sim 13.1%, and \sim 1 × 10⁻¹⁵ s⁻¹, respectively. The total throw and mean throw rate of the basin-bounding LSF are 2,281 ± 62 m and 0.54 ± 0.01 km/Myr, respectively.
- 3. The basin depths and the onsets of sedimentation are 440.9 m and ~6.1 Ma at borehole ZK1 and 1,370.3 m and ~4.2 Ma at ZK3. Such basin configuration of more subsidence at the younger site indicates the uneven basin depths are controlled by the differential throw rates of the LSF rather than differential onsets of faulting.
- 4. The basin depths increasing northward indicates its extension increasing northward and thus the clockwise rotation of the basin controlled by right-lateral transtensional shear. The rotation patterns of the LB and other circum-Ordos basins provide new evidence of right-lateral transtensional deformation of the SRS and the craton-scale rigid transtensional bookshelf faulting model of North China. We find that the kinematic patterns of the circum-Ordos basins are controlled by basin-scale non-rigid transtensional bookshelf faulting.
- 5. We infer the inherited structures weakened the cratonic lithosphere and significantly influenced the tectonic evolution of the LB. Inherited crustal weakness, low extension rate, and lower lithosphere counterflow all govern the basin evolution, which provides new insights into the tectonic mechanisms for the magma-poor SRS.

Data Availability Statement

The original cosmogenic data and seismic profile used in this study can be found in Su (2022) (DOI, https://doi.org/10.17605/OSF.IO/K8TS5). Previous borehole data were from National Geological Drilling Database Service Platform (Cores and Samples Center of Natural Resources, China Geological Survey, 2014), available at https://zk.cgsi.cn/ (retrieved date January 2021). Quantitative structural modeling used commercial software StructureSolver version 4.2 (Nunns and Rogan LLC, 2009), available under the StructureSolver license at https://www.structuresolver.com/.

References

Allen, M. B., Macdonald, D. I. M., Xun, Z., Vincent, S. J., & Brouet-Menzies, C. (1997). Early Cenozoic two-phase extension and late Cenozoic thermal subsidence and inversion of the Bohai Basin, northern China. *Marine and Petroleum Geology*, 14(7–8), 951–972. https://doi.org/10.1016/S0264-8172(97)00027-5

Bassi, G. (1991). Factors controlling the style of continental rifting: Insights from numerical modelling. *Earth and Planetary Science Letters*, 105(4), 430–452. https://doi.org/10.1016/0012-821X(91)90183-I

Bassi, G. (1995). Relative importance of strain rate and rheology for the mode of continental extension. *Geophysical Journal International*, 122(1), 195–210. https://doi.org/10.1111/j.1365-246X.1995.tb03547.x

Acknowledgments

We thank Yan Ma, Weiheng Zhang, Ping Wang, and Yifang Chen for helpful discussion, and Wen Sun, Chao Zhou, Wei Li, Xiao Sun, and Xiaobing Yan for field assistance. The manuscript benefits greatly from reviews by Mohamed Gouiza and two anonymous reviewers. The seismic section is courtesy of Zihong Li. The three new boreholes were drilled by the Shanxi Provincial Geological Prospecting Bureau, China. This work is supported by the Basic Research Fund from Institute of Geology, China Earthquake Administration (Grants IGCEA2021, IGCEA1416); Shanxi Taiyuan Continental Rift Dynamics National Observation and Research Station (Grant NORSTY20-03); National Natural Science Foundation of China (Grants U1939201, 42002232), Peng Su was sponsored as an Academic Visiting Scholar at Oregon State University by the China Scholarship Council (File No. 201704190013).

SU ET AL. 18 of 22

Tectonics

- Beaumont, C., & Ings, S. J. (2012). Effect of depleted continental lithosphere counterflow and inherited crustal weakness on rifting of the continental lithosphere: General results. *Journal of Geophysical Research*, 117(B8), B08407. https://doi.org/10.1029/2012JB009203
- Bellier, O., Mercier, J. L., Vergely, P., Long, C., & Ning, C. (1988). Evolution sedimentaire et tectonique du graben cenozoique de la Wei He (Province du Shaanxi, Chine du Nord). Bulletin de la Societe Geologique de France, 4(6), 979–994. https://doi.org/10.2113/gssgfbull.iv.6.979
- Bi, Y., Pang, E., Sun, Y., Liu, Y., Bian, Q., Liu, S., et al. (2022). Magnetostratigraphy of the fluvio-lacustrine sequence of core DY-1 in the Datong Basin and its implications for the evolution of the Shanxi Rift System in northern China. *Palaeogeography, Palaeoclimatology, Palaeoecology*, 599, 111063. https://doi.org/10.1016/j.palaeo.2022.111063
- Brun, J.-P. (1999). Narrow rifts versus wide rifts: Inferences for the mechanics of rifting from laboratory experiments. *Philosophical Transactions of the Royal Society, Series A*, 357(1753), 695–712. https://doi.org/10.1098/rsta.1999.0349
- Brune, S., Popov, A. A., & Sobolev, S. V. (2012). Modeling suggests that oblique extension facilitates rifting and continental break-up. *Journal of Geophysical Research*, 117(B8), B08402. https://doi.org/10.1029/2011JB008860
- Buck, W. R. (1991). Modes of continental lithospheric extension. Journal of Geophysical Research, 96(B12), 20161–20178. https://doi.org/10.1029/91JB01485
- Buck, W. R. (2004). Consequences of asthenospheric variability on continental rifting. In G. D. Karner, B. Taylor, N. W. Droscoll, & D. L. Kohlstedt (Eds.), Rheology and deformation of the lithosphere at continental margins (pp. 1–30). Columbia University Press. https://doi.org/10.7312/karn12738-002
- Cai, Y., Wu, J., Rietbrock, A., Wang, W., Fang, L., Yi, S., & Liu, J. (2021). S wave velocity structure of the crust and upper mantle beneath Shanxi rift, central North China Craton and its tectonic implications. *Tectonics*, 40(4), e2020TC006239. https://doi.org/10.1029/2020TC006239
- Chen, L., Jiang, M., Yang, J., Wei, Z., Liu, C., & Ling, Y. (2014). Presence of an intralithospheric discontinuity in the central and western North China Craton: Implications for destruction of the craton. *Geology*, 42(3), 223–226. https://doi.org/10.1130/G35010.1
- Chen, X., Dong, S., Shi, W., Zuza, A. V., Li, Z., Chen, P., et al. (2021). Magnetostratigraphic ages of the cenozoic Weihe and Shanxi Grabens in North China and their tectonic implications. *Tectonophysics*, 813, 228914. https://doi.org/10.1016/j.tecto.2021.228914
- Cheng, F., Jolivet, M., Dupont-Nivet, G., Wang, L., Yu, X., & Guo, Z. (2015). Lateral extrusion along the Altyn Tagh Fault, Qilian Shan (NE Tibet): Insight from a 3D crustal budget. *Terra Nova*, 27(6), 416–425. https://doi.org/10.1111/ter.12173
- Chmeleff, J., Blanckenburg, F., Kossert, K., & Jakob, D. (2010). Determination of the ¹⁰Be half-life by multicollector ICP-MS and liquid scintillation counting. *Nuclear Instruments and Methods in Physics Research Section B: Beam Interactions with Materials and Atoms*, 268(2), 192–199. https://doi.org/10.1016/j.nimb.2009.09.012
- Clinkscales, C., & Kapp, P. (2019). Structural style and kinematics of the Taihang-Luliangshan fold belt, North China: Implications for the Yanshanian orogeny. *Lithosphere*, 11(6), 767–783. https://doi.org/10.1130/L1096.1
- Clinkscales, C., Kapp, P., Thomson, S., Wang, H., Laskowski, A., Orme, D. A., & Pullen, A. (2021). Regional exhumation and tectonic history of the Shanxi Rift and Taihangshan, North China. *Tectonics*, 40(3), e2020TC006416. https://doi.org/10.1029/2020TC006416
- Cores and Samples Center of Natural Resources, China Geological Survey. (2014). National Geological Drilling Database Service Platform Retrieved from https://zk.cgsi.cn/
- Corti, G., Calignano, E., Petit, C., & Sani, F. (2011). Controls of lithospheric structure and plate kinematics on rift architecture and evolution: An experimental modeling of the Baikal Rift. *Tectonics*, 30(3), TC3011. https://doi.org/10.1029/2011TC002871
- D'Agostino, N., Chamot-Rooke, N., Funiciello, R., Jolivet, L., & Speranza, F. (1998). The role of pre-existing thrust faults and topography on the styles of extension in the Gran Sasso range (central Italy). *Tectonophysics*, 292(3–4), 229–254. https://doi.org/10.1016/S0040-1951(98)00070-5
- Davis, G. A., Zheng, Y., Wang, C., Darby, B. J., Zhang, C., & Gehrels, G. (2001). Mesozoic tectonic evolution of the Yanshan fold and thrust belt, with emphasis on Hebei and Liaoning provinces, northern China. In M. S. Hendrix & G. A. Davis (Eds.), *Paleozoic and mesozoic tectonic evolution of central and eastern Asia: From continental assembly to intracontinental deformation* (Vol. 194, pp. 171–198). Memoir-Geological Society of America.
- Deng, Q., Su, Z., Wang, T., & Xu, X. (1993). The basic characteristic of the seismogenic structure and the zonation of the potential seismic zone in the Linfen basin. In Z. Ma (Ed.), *Earthquake research and systematic disaster reduction of Linfen, Shanxi* (pp. 67–95). Seismological Press. (in Chinese).
- Dias, A. E. S., Lavier, L., & Hayman, N. W. (2015). Conjugate rifted margins width and asymmetry: The interplay between lithospheric strength and thermomechanical processes. *Journal of Geophysical Research: Solid Earth*, 120(12), 8672–8700. https://doi.org/10.1002/2015JB012074
- Dong, S., Zhang, Y., Long, C., Yang, Z., Ji, Q., Tao, W., et al. (2008). Jurassic tectonic revolution in China and new interpretation of the "Yanshan movement". Acta Geologica Sinica, 82(2), 334–347. https://doi.org/10.1111/j.1755-6724.2008.tb00583.x
- Dou, L., Yao, H., Fang, L., Luo, S., Song, M., Yan, X., & Cheng, C. (2021). High-resolution crustal velocity structure in the Shanxi rift zone and its tectonic implications. *Science China Earth Sciences*, 64(5), 728–743. https://doi.org/10.1007/s11430-020-9710-x
- Dunbar, J. A., & Sawyer, D. S. (1988). Continental rifting at pre-existing lithospheric weaknesses. *Nature*, 333(6172), 450–452. https://doi.org/10.1038/333450a0
- Eichelberger, N. W., Hughes, A. N., & Nunns, A. G. (2015). Combining multiple quantitative structural analysis techniques to create robust structural interpretations. *Interpretation*, 3(4), SAA89–SAA104. https://doi.org/10.1190/INT-2015-0016.1
- England, P. (1983). Constraints on extension of continental lithosphere. *Journal of Geophysical Research*, 88(B2), 1145–1152. https://doi.org/10.1029/JB088iB02p01145
- Faccenna, C., Nalpas, T., Brun, J.-P., Davy, P., & Bosi, V. (1995). The influence of pre-existing thrust faults on normal fault geometry in nature and in experiments. *Journal of Structural Geology*, 17(8), 1139–1149. https://doi.org/10.1016/0191-8141(95)00008-2
- Fan, L.-G., Meng, Q.-R., Wu, G.-L., Wei, H.-H., Du, Z.-M., & Wang, E. (2019). Paleogene crustal extension in the eastern segment of the NE Tibetan plateau. Earth and Planetary Science Letters, 514, 62–74. https://doi.org/10.1016/j.epsl.2019.02.036
- Fan, S., Zhang, T., Chen, S., & Li, R. (2020). New findings regarding the Fen-Wei Graben on the southeastern margin of the Ordos Block: Evidence from the Cenozoic sedimentary record from the borehole. *Geological Journal*, 55(12), 7581–7593. https://doi.org/10.1002/gj.3815
- Gouiza, M., & Naliboff, J. (2021). Rheological inheritance controls the formation of segmented rifted margins in cratonic lithosphere. *Nature Communications*, 12(1), 4653. https://doi.org/10.1038/s41467-021-24945-5
- Granger, D. E., Gibbon, R. J., Kuman, K., Clarke, R. J., Bruxelles, L., & Caffee, M. W. (2015). New cosmogenic burial ages for Sterkfontein member 2 *Australopithecus* and Member 5 Oldowan. *Nature*, 522(7554), 85–88. https://doi.org/10.1038/nature14268
- Granger, D. E., Kirchner, J. W., & Finkel, R. C. (1997). Quaternary downcutting rate of the New River, Virginia, measured from differential decay of cosmogenic ²⁶Al and ¹⁰Be in cave-deposited alluvium. *Geology*, 25(2), 107–110. https://doi.org/10.1130/0091-7613(1997)025<010 7:QDROTN>2.3.CO;2
- Granger, D. E., & Muzikar, P. F. (2001). Dating sediment burial with in situ-produced cosmogenic nuclides: Theory, techniques, and limitations. Earth and Planetary Science Letters, 188(1–2), 269–281. https://doi.org/10.1016/S0012-821X(01)00309-0

SU ET AL. 19 of 22

Tectonics

- Hao, M., Wang, Q., Cui, D., Liu, L., & Zhou, L. (2016). Present-day crustal vertical motion around the Ordos block constrained by precise leveling and GPS data. Surveys in Geophysics, 37(5), 923–936. https://doi.org/10.1007/s10712-016-9375-1
- Hao, M., Wang, Q., Zhang, P., Li, Z., Li, Y., & Zhuang, W. (2021). "Frame Wobbling" causing crustal deformation around the Ordos Block. Geophysical Research Letters, 48(1), e2020GL091008. https://doi.org/10.1029/2020GL091008
- Heberer, B., Anzenbacher, T., Neubauer, F., Genser, J., Dong, Y., & Dunkl, I. (2014). Polyphase exhumation in the western Qinling Mountains, China: Rapid Early Cretaceous cooling along a lithospheric-scale tear fault and pulsed Cenozoic uplift. *Tectonophysics*, 617, 31–43. https://doi.org/10.1016/j.tecto.2014.01.011
- Hopper, E., Gaherty, J. B., Shillington, D. J., Accardo, N. J., Nyblade, A. A., Holtzman, B. K., et al. (2020). Preferential localized thinning of lithospheric mantle in the melt-poor Malawi Rift. Nature Geoscience, 13(8), 584–589. https://doi.org/10.1038/s41561-020-0609-y
- Huismans, R. S., & Beaumont, C. (2003). Symmetric and asymmetric lithospheric extension: Relative effects of frictional-plastic and viscous strain softening. *Journal of Geophysical Research*, 108(B10), 2496. https://doi.org/10.1029/2002JB002026
- Ivanov, A. V., Demonterova, E. I., He, H., Perepelov, A. B., Travin, A. V., & Lebedev, V. A. (2015). Volcanism in the Baikal Rift: 40 years of active-versus-passive model discussion. Earth-Science Reviews, 148, 18–43. https://doi.org/10.1016/j.earscirev.2015.05.011
- Kolawole, F., Phillips, T. B., Atekwana, E. A., & Jackson, C. A. L. (2021). Structural inheritance controls strain distribution during early continental rifting, Rukwa Rift. Frontiers in Earth Science, 9, 707869. https://doi.org/10.3389/feart.2021.707869
- Korschinek, G., Bergmaier, A., Faestermann, T., Gerstmann, U. C., Knie, K., Rugel, G., et al. (2010). A new value for the half-life of ¹⁰Be by Heavy-Ion Elastic Recoil Detection and liquid scintillation counting. Nuclear Instruments and Methods in Physics Research Section B: Beam Interactions with Materials and Atoms, 268(2), 187–191. https://doi.org/10.1016/j.nimb.2009.09.020
- Lal, D., & Arnold, J. R. (1985). Tracing quartz through the environment. Proceedings of the Indian Academy of Sciences Earth & Planetary Sciences, 94, 1–5. https://doi.org/10.1007/bf02863403
- Li, S., Lai, X., Liu, B., Wang, Z., He, J., & Sun, Y. (2011). Differences in lithospheric structures between two sides of Taihang Mountain obtained from the Zhucheng-Yichuan deep seismic sounding profile. Science China Earth Sciences, 54(6), 871–880. https://doi.org/10.1007/ s11430-011-4191-4
- Li, Z., Liu, B., Yuan, H., Feng, S., Chen, W., Li, W., & Kou, K. (2014). Fine crustal structure and tectonics of Linfen Basin—From the results of seismic reflection profile. *Chinese Journal of Geophysics*, 57(5), 1487–1497. (in Chinese with English abstract). https://doi.org/10.6038/cjg20140513
- Lifton, N., Sato, T., & Dunai, T. J. (2014). Scaling in situ cosmogenic nuclide production rates using analytical approximations to atmospheric cosmic-ray fluxes. Earth and Planetary Science Letters, 386, 149–160. https://doi.org/10.1016/j.epsl.2013.10.052
- Ling, Y., Chen, L., Wei, Z., Jiang, M., & Wang, X. (2017). Crustal S-velocity structure and radial anisotropy beneath the southern part of central and western North China Craton and the adjacent Qilian Orogenic Belt from ambient noise tomography. Science China Earth Sciences, 60(10), 1752–1768. https://doi.org/10.1007/s11430-017-9092-8
- Liu, J., Zhang, P., Lease, R. O., Zheng, D., Wan, J., Wang, W., & Zhang, H. (2013). Eocene onset and late Miocene acceleration of Cenozoic intracontinental extension in the North Qinling range—Weihe graben: Insights from apatite fission track thermochronology. *Tectonophysics*, 584, 281–296. https://doi.org/10.1016/j.tecto.2012.01.025
- Liu, J., Zhang, P., Zheng, D., Wan, J., Wang, W., Du, P., & Lei, Q. (2010). Pattern and timing of late Cenozoic rapid exhumation and uplift of the Helan Mountain, China. Science China Earth Sciences, 53(3), 345–355. https://doi.org/10.1007/s11430-010-0016-0
- Liu, Y., Li, L., van Wijk, J., Li, A., & Fu, Y. V. (2021). Surface-wave tomography of the Emeishan large igneous province (China): Magma storage system, hidden hotspot track, and its impact on the Capitanian mass extinction. Geology, 49(9), 1032–1037. https://doi.org/10.1130/G49055.1
- Liu, Y., Murphy, M. A., van Wijk, J., Koning, D. J., Smith, T., & Andrea, R. A. (2019). Progressive opening of the northern Rio Grande rift based on fault structure and kinematics of the Tusas-Abiquiu segment in north-central New Mexico, US. *Tectonophysics*, 753, 15–35. https://doi. org/10.1016/j.tecto.2019.01.004
- Manatschal, G., Chenin, P., Lescoutre, R., Miró, J., Cadenas, P., Saspiturry, N., et al. (2021). The role of inheritance in forming rifts and rifted margins and building collisional orogens: A Biscay-Pyrenean perspective. Bulletin de la Société Géologique de France, 192(1), 55. https://doi.org/10.1051/bsgf/2021042
- McKenzie, D. (1978). Some remarks on the development of sedimentary basins. Earth and Planetary Science Letters, 40(1), 25–32. https://doi.org/10.1016/0012-821X(78)90071-7
- Meng, Q.-R., Wei, H.-H., Qu, Y.-Q., & Ma, S.-X. (2011). Stratigraphic and sedimentary records of the rift to drift evolution of the northern North China craton at the Paleo- to Mesoproterozoic transition. *Gondwana Research*, 20(1), 205–218. https://doi.org/10.1016/j.gr.2010.12.010 Molnar, P., & Tapponnier, P. (1975). Cenozoic tectonics of Asia: Effects of a continental collision. *Science*, 189(4201), 419–426. https://doi.org/10.1126/science.189.4201.419
- Morley, C. K. (2010). Stress re-orientation along zones of weak fabrics in rifts: An explanation for pure extension in 'oblique' rift segments? Earth and Planetary Science Letters, 297(3–4), 667–673. https://doi.org/10.1016/j.epsl.2010.07.022
- Morley, C. K., Haranya, C., Phoosongsee, W., Pongwapee, S., Kornsawan, A., & Wonganan, N. (2004). Activation of rift oblique and rift parallel pre-existing fabrics during extension and their effect on deformation style: Examples from the rifts of Thailand. *Journal of Structural Geology*, 26(10), 1803–1829. https://doi.org/10.1016/j.jsg.2004.02.014
- Muirhead, J. D., Kattenhorn, S. A., Lee, H., Mana, S., Turrin, B. D., Fischer, T. P., et al. (2016). Evolution of upper crustal faulting assisted by magmatic volatile release during early-stage continental rift development in the East African Rift. *Geosphere*, 12(6), 1670–1700. https://doi.org/10.1130/GES01375.1
- Nishiizumi, K. (2004). Preparation of ²⁶Al AMS standards. *Nuclear Instruments and Methods in Physics Research Section B: Beam Interactions with Materials and Atoms*, 223–224, 388–392. https://doi.org/10.1016/j.nimb.2004.04.075
- Nishiizumi, K., Imamura, M., Caffee, M. W., Southon, J. R., Finkel, R. C., & McAninch, J. (2007). Absolute calibration of ¹⁰Be AMS standards. Nuclear Instruments and Methods in Physics Research Section B: Beam Interactions with Materials and Atoms, 258(2), 403–413. https://doi.org/10.1016/j.nimb.2007.01.297
- Nunns, & Rogan, L. L. C. (2009). StructureSolver: Practical structural geology tools for interpreters (version 4.2) [Software]. StructureSolver. Retrieved from https://www.structuresolver.com/s
- Peace, A., McCaffrey, K., Imber, J., van Hunen, J., Hobbs, R., & Wilson, R. (2018). The role of pre-existing structures during rifting, continental breakup and transform system development, offshore West Greenland. Basin Research, 30(3), 373–394. https://doi.org/10.1111/bre.12257
- Pedersen, T., & Ro, H. E. (1992). Finite duration extension and decompression melting. Earth and Planetary Science Letters, 113(1–2), 15–22. https://doi.org/10.1016/0012-821X(92)90208-D
- Peltzer, G., Tapponnier, P., Zhang, Z., & Xu, Z. (1985). Neogene and Quaternary faulting in and along the Qinling Shan. *Nature*, 317(6037), 500–505. https://doi.org/10.1038/317500a0

SU ET AL. 20 of 22

- Petit, C., & Déverchère, J. (2006). Structure and evolution of the Baikal Rift: A synthesis. Geochemistry, Geophysics, Geosystems, 7(11), Q11016. https://doi.org/10.1029/2006GC001265
- Ren, J., Tamaki, K., Li, S., & Junxia, Z. (2002). Late Mesozoic and Cenozoic rifting and its dynamic setting in Eastern China and adjacent areas. Tectonophysics, 344(3-4), 175–205. https://doi.org/10.1016/S0040-1951(01)00271-2
- Ren, Z., Qi, K., Liu, R., Cui, J., Chen, Z., Zhang, Y., et al. (2020). Dynamic background of Early Cretaceous tectonic thermal events and its control on various mineral accumulations such as oil and gas in the Ordos Basin. Acta Petrologica Sinica, 36(4), 1213–1234. (in Chinese with English abstract). https://doi.org/10.18654/1000-0569/2020.04.15
- Shanxi Provincial Geological Exploration Bureau, P.R. China (SPGEB). (1975–1978). Geological maps of the Linfen, Qinyuan, Houma, and Jincheng (scale 1: 200,000). Geological Publishing House. (in Chinese).
- Shi, W., Dong, S., & Hu, J. (2020). Neotectonics around the Ordos block, North China: A review and new insights. *Earth-Science Reviews*, 200, 102969. https://doi.org/10.1016/j.earscirev.2019.102969
- Shu, P., Xu, X., Feng, S., Liu, B., Li, K., Tapponnier, P., et al. (2023). Sedimentary and tectonic evolution of the Banquan pull-apart basin and implications for late Cenozoic dextral strike-slip movement of the Tanlu Fault Zone. *Science China Earth Sciences*, 66(4), 797–820. https://doi.org/10.1007/s11430-022-1028-5
- State Seismological Bureau (SSB). (1988). Active Fault system around Ordos Massif. Seismological Press. (in Chinese).
- Su, P. (2022). Original cosmogenic data and seismic profile used to quantify the structure and extension rate of the Linfen Basin, Shanxi Rift System since the latest Miocene [Dataset]. OSF. https://doi.org/10.17605/OSF.IO/K8TS5
- Su, P., He, H., Tan, X., Liu, Y., Shi, F., & Kirby, E. (2021). Initiation and evolution of the Shanxi Rift System in North China: Evidence from low-temperature thermochronology in a plate reconstruction framework. *Tectonics*, 40(3), e2020TC006298. https://doi.org/10.1029/2020TC006298
- Tang, Y., Feng, Y., Chen, Y., Zhou, S., Ning, J., Wei, S., et al. (2010). Receiver function analysis at Shanxi Rift. *Chinese Journal of Geophysics*, 53(9), 2102–2109. (in Chinese with English abstract). https://doi.org/10.3969/j.issn.0001-5733.2010.09.010
- Tang, Y.-J., Zhang, H.-F., & Ying, J.-F. (2006). Asthenosphere–lithospheric mantle interaction in an extensional regime: Implication from the geochemistry of Cenozoic basalts from Taihang Mountains, North China Craton. Chemical Geology, 233(3–4), 309–327. https://doi. org/10.1016/j.chemgeo.2006.03.013
- Tetreault, J. L., & Buiter, S. J. H. (2018). The influence of extension rate and crustal rheology on the evolution of passive margins from rifting to break-up. *Tectonophysics*, 746, 155–172. https://doi.org/10.1016/j.tecto.2017.08.029
- Thybo, H., & Artemieva, I. M. (2013). Moho and magmatic underplating in continental lithosphere. *Tectonophysics*, 609, 605–619. https://doi.org/10.1016/j.tecto.2013.05.032
- Thybo, H., Maguire, P. K. H., Birt, C., & Perchuć, E. (2000). Seismic reflectivity and magmatic underplating beneath the Kenya Rift. *Geophysical Research Letters*, 27(17), 2745–2748. https://doi.org/10.1029/1999GL011294
- Ulvrova, M. M., Brune, S., & Williams, S. (2019). Breakup without borders: How continents speed up and slow down during rifting. *Geophysical Research Letters*, 46(3), 1338–1347. https://doi.org/10.1029/2018GL080387
- van Wijk, J. W., & Cloetingh, S. A. P. L. (2002). Basin migration caused by slow lithospheric extension. Earth and Planetary Science Letters, 198(3–4), 275–288. https://doi.org/10.1016/S0012-821X(02)00560-5
- Wang, W., Kirby, E., Zhang, P., Zheng, D., Zhang, G., Zhang, H., et al. (2013). Tertiary basin evolution along the northeastern margin of the Tibetan Plateau: Evidence for basin formation during Oligocene transtension. *Bulletin of the Geological Society of America*, 125(3–4), 377–400. https://doi.org/10.1130/B30611.1
- Wang, Z., Zhang, P., Garzione, C. N., Lease, R. O., Zhang, G., Zheng, D., et al. (2012). Magnetostratigraphy and depositional history of the Miocene Wushan basin on the NE Tibetan plateau, China: Implications for middle Miocene tectonics of the West Qinling fault zone. *Journal of Asian Earth Sciences*, 44, 189–202. https://doi.org/10.1016/j.jseaes.2011.06.009
- Wei, R., Zhuang, Q., Yan, J., Wei, Y., Du, Y., & Fan, J. (2022). Late cenozoic stratigraphic division and sedimentary environment of Jinzhong Basin in Shanxi province, with the climate and lake evolution since the pre-Qin period. *Geology in China*, 49(3), 912–928. (in Chinese with English abstract)
- Wei, Z., Chen, L., & Xu, W. (2011). Crustal thickness and Vp/Vs ratio of the central and western North China Craton and its tectonic implications. *Geophysical Journal International*, 186(2), 385–389. https://doi.org/10.1111/j.1365-246X.2011.05089.x
- Wilson, D., Aster, R., West, M., Ni, J., Grand, S., Gao, W., et al. (2005). Lithospheric structure of the Rio Grande Rift. *Nature*, 433(7028), 851–855. https://doi.org/10.1038/nature03297
- Wu, F.-Y., Yang, J.-H., Xu, Y.-G., Wilde, S. A., & Walker, R. J. (2019). Destruction of the North China craton in the mesozoic. *Annual Review of Earth and Planetary Sciences*, 47(1), 173–195. https://doi.org/10.1146/annurev-earth-053018-060342
- Xiao, H., & Suppe, J. (1992). Origin of rollover. AAPG Bulletin, 76(4), 509-529.
- Xu, X., & Ma, X. (1992). Geodynamics of the Shanxi rift system, China. Tectonophysics, 208(1–3), 325–340. https://doi. org/10.1016/0040-1951(92)90353-8
- Xu, X., Ma, X., & Deng, Q. (1993). Neotectonic activity along the Shanxi rift system, China. Tectonophysics, 219(4), 305–325. https://doi.org/10.1016/0040-1951(93)90180-R
- Xu, Y., He, H., Deng, Q., Allen, M. B., Sun, H., & Bi, L. (2018). The CE 1303 Hongdong Earthquake and the Huoshan Piedmont Fault, Shanxi Graben: Implications for magnitude limits of normal fault Earthquakes. *Journal of Geophysical Research: Solid Earth*, 123(4), 3098–3121. https://doi.org/10.1002/2017JB014928
- Yang, Y., Zhao, J., Liu, C., Xue, R., & Yan, Z. (2017). The Zircon LA-ICP-MS U-Pb ages and geochemical characteristics of Ta'ershan intrusions, southern Shanxi province, and their geological implications. Geological Review, 63(3), 809–821. https://doi.org/10.16509/j.georeview.2017.03.019
- Yin, A. (2010). Cenozoic tectonic evolution of Asia: A preliminary synthesis. Tectonophysics, 488(1–4), 293–325. https://doi.org/10.1016/j.tecto.2009.06.002
- Yin, A., & Ingersoll, R. V. (1997). A model for evolution of Laramide axial basins in the Southern Rocky Mountains, USA. International Geology Review, 39(12), 1113–1123. https://doi.org/10.1080/00206819709465318
- Yin, Y., Jin, S., Wei, W., Ye, G., Jing, J., Zhang, L., et al. (2017). Lithospheric rheological heterogeneity across an intraplate rift basin (Linfen Basin, North China) constrained from magnetotelluric data: Implications for seismicity and rift evolution. *Tectonophysics*, 717, 1–15. https://doi.org/10.1016/j.tecto.2017.07.014
- Zhang, B., Zhang, J., Qu, J., Zhao, H., Wang, Y., Li, J., et al. (2021). Lüliangshan: A mesozoic basement involved fold system in the Central North China craton. *Earth Science*, 46(7), 2423–2448. (in Chinese with English abstract). https://doi.org/10.3799/dqkx.2020.235
- Zhang, Y., Chen, L., Ai, Y., & Jiang, M. (2019). Lithospheric structure beneath the central and western North China Craton and adjacent regions from S-receiver function imaging. *Geophysical Journal International*, 219(1), 619–632. https://doi.org/10.1093/gji/ggz322

SU ET AL. 21 of 22

- Zhao, B., Zhang, C., Wang, D., Huang, Y., Tan, K., Du, R., & Liu, J. (2017). Contemporary kinematics of the Ordos block, North China and its adjacent rift systems constrained by dense GPS observations. *Journal of Asian Earth Sciences*, 135, 257–267. https://doi.org/10.1016/j.jseaes.2016.12.045
- Zhao, G., Sun, M., Wilde, S. A., & Sanzhong, L. (2005). Late Archean to Paleoproterozoic evolution of the North China craton: Key issues revisited. *Precambrian Research*, 136(2), 177–202. https://doi.org/10.1016/j.precamres.2004.10.002
- Zhao, G., Wilde, S. A., Sun, M., Li, S., Li, X., & Zhang, J. (2008). SHRIMP U–Pb zircon ages of granitoid rocks in the Lüliang Complex: Implications for the accretion and evolution of the Trans-North China Orogen. *Precambrian Research*, 160(3–4), 213–226. https://doi.org/10.1016/j.precamres.2007.07.004
- Zhao, H., Zhang, J., Qu, J., Zhang, B., Yun, L., Li, J., et al. (2020). Nature of the eastern boundary of the mesozoic Ordos Basin and the formation of the Lüliangshan anticline. *The Journal of Geology*, 128(2), 157–187. https://doi.org/10.1086/707346
- Zhao, J., Sheng, S., Wang, D., Lu, J., Zhang, J., Liu, G., & Cui, H. (2019). Analysis on evolution, modification and hydrocarbon resources potential of the upper Paleozoic in the Linfen-Yuncheng basin. *Geological Review*, 65(1), 168–180. (in Chinese with English abstract). https://doi.org/10.16509/j.georeview.2019.01.011
- Zhou, H.-W. (2014). Practical seismic data analysis (p. 481). Cambridge University Press.
- Zhu, R., Chen, L., Wu, F., & Liu, J. (2011). Timing, scale and mechanism of the destruction of the North China Craton. Science China Earth Sciences, 54(6), 789–797. https://doi.org/10.1007/s11430-011-4203-4
- Zuza, A. V., & Yin, A. (2016). Continental deformation accommodated by non-rigid passive bookshelf faulting: An example from the Cenozoic tectonic development of northern Tibet. *Tectonophysics*, 677–678, 227–240. https://doi.org/10.1016/j.tecto.2016.04.007

SU ET AL. 22 of 22